Seismic Determination of Reservoir Heterogeneity: Application to the Characterization of Heavy Oil Reservoirs

Annual Report

Report Period: 09/01/2001 - 08/31/2002

Matthias G. Imhof

December 2002

DE-FC26-00BC15301

Matthias G. Imhof

Department of Geological Sciences

Virgina Tech

4044 Derring Hall (0420)

Blacksburg, VA 24061

James W. Castle

Department of Geological Sciences

Clemson University

340 Brackett Hall

Clemson, SC 29634-0976

Disclaimer

Abstract

The objective of the project is to examine how seismic and geologic data can be used to improve characterization of small-scale heterogeneity and their parameterization in reservoir models. The study is performed at West Coalinga Field in California.

We are currently in the process of determining the limits of current state-of-the-art interpretation methods for poststack seismic data. We developed and applied three-dimensional seismic attributes which estimate the statistics of seismic heterogeneity. We just formulated an algorithm to infer parameters of object-based reservoir models from seismic data, and now, we are testing the method with synthetic reservoir data. Lastly, we built models of reservoir heterogeneity for two focus areas in Coalinga field using plentiful wireline data.

Contents

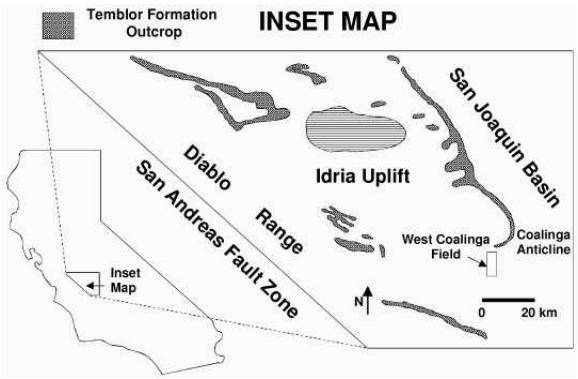

Figure 1: Location map of the Coalinga area, California.

1 Introduction

The objective of the project is to examine how seismic data can be used to parameterize models of small-scale reservoir heterogeneity. Although these heterogeneities cannot be resolved individually (deterministically) using seismic data, one can at least attempt to estimate their statistical properties from seismic data.

Reservoir characterization is an essential step in delineation, development, and production of hydrocarbon reserves. Our test area, the giant Coalinga field in California's San Joaquin Valley, is a good example. Large-scale steam-flood projects have been utilized for many years in order to enhance recovery of heavier oil. Steam-floods are costly to operate due to the necessary infrastructure and their energy consumption. Optimally, injected steam would spread evenly from the injection point and push the oil toward the producer wells. In reality, the steam patterns are very complex. Reservoir characterization provides an improved understanding of the reservoir and the movement of steam, which will help to increase the profitability by reducing steam injection which decreases the environmental impact of steam injection. Reservoir heterogeneity affects not only the steam flood, but also the production. The Coalinga reservoirs are strongly compartmentalized which is aggravated by the high oil viscosity. Reservoir characterization helps siting infill wells to produce bypassed oil to increase ultimate recovery.

Knowing the details of the reservoir allows simulation of different injection or production scenarios. The problem, however, is to build an accurate and suitable reservoir model that includes small-scale heterogeneity. Locally, boreholes yield an excellent description of the vertical heterogeneity at different spatial scales ranging from centimeters to hundreds of meters. Most of the time, the lateral heterogeneity cannot be derived from well data because of the large distances between wells. The most abundant data are seismic data, but their resolution is only on the order of tens of meters which is typically insufficient to resolve geological heterogeneities. Features smaller than a seismic quarter wavelength cannot be resolved with certainty. Yet the geology exhibits many small-scale features which may have a pronounced effect on the reservoir. For example, a clay drape is invisible on the seismic data but poses an impenetrable barrier to steam and oil. By combining seismic and well data, a deterministic framework is traditionally constructed which contains the major stratigraphic features. Small-scale features are filled in using statistical methods conditioned to well data and outcrops. The parameters for the fill-in process are often provided by measurements of analogous outcropping formations, analogous mature reservoirs with a dense well spacing, horizontal wells, pressure and production tests, or simply by accepting the default parameters of the modeling packet.

The objective of the project is to examine how seismic and geologic data can be used to describe small-scale heterogeneity and parameterize the reservoir models. Although these heterogeneities cannot be resolved individually (deterministically) using seismic data, we attempt to estimate their statistics from seismic data. The Coalinga field contains more than 2000 wells which provide the unusual luxury that even small-scale heterogeneity can be characterized with well data. The site allows construction of reservoir models from either seismic data or wireline logs and outcrops. Since these data are independent, the models can be compared and validated against each other. Ultimately, integration of seismic and geologic data and models will lead to a new level of understanding of the complex Coalinga field.

2 Executive Summary

The objective of the project is to examine how seismic data can be used to improve characterization of small-scale heterogeneity and their parameterization in reservoir models. During the second year, we interpreted the seismic poststack data, developed a seismic 3-D attribute which estimates seismic heterogeneity, developed an inversion algorithm to estimate the parameters of reservoir models based on geometric objects from seismic data, and performed two geologic heterogeneity studies.

We tied the seismic data to wireline logs and mapped the four Temblor unconformities seismically. Multiple generations of channel-like features are cut, deposited, and stacked which render identification of unconformities difficult. Furthermore, we observed that the middle unconformities are merging in portions of the field indicating an extended time period of erosion. We expect that seismic volume visualization and geobody analysis will resolve these delineation problems.

We developed a family of seismic attributes which estimate degree and orientation of local heterogeneity in the seismic data. This seismic heterogeneity may be related to lithologic heterogeneity in the reservoir. We observed that their statistics are highly variable within the seismic focus area of $4,400 \times 1,400$ m. The characteristic lengths of seismic heterogeneities range from 400 to $1,000$ m predominantely aligned in the north-south direction.

Object-based reservoir models build realizations by emplacing geometric objects corresponding to channels, barriers, or sand sheets. We developed a new algorithm to estimate the object parameters from seismic data. Tests with synthetic data were very encouraging. We are just beginning preliminary application with seismic field data, although further testing and validation will be necessary.

Finally, we used core descriptions, wireline logs, and outcrop data to develop 3-D reservoir models for two focus sites. At each site, we applied four different modeling methods and compared their results against each other, core descriptions, and wireline data. We concluded that stochastic or conditioned models will be best suited for integration with seismic data.

In the third and final project year, we will perform geobody analysis based on volume visualization, apply the object-parameter inversion, and integrate seismic and geologic models of reservoir heterogeneity.

3 Cummulative Bibliography

M. G. Imhof, 'The Heterogeneity Cube: a Family of Seismic Attributes', 71st Annual Internat. Mtg., Soc. Expl. Geophys., Expanded Abstracts, 2001.

M. G. Imhof, 'The Heterogeneity Cube: a Family of Seismic Attributes', AAPG Annual Convention, Expanded Abstracts, 2002.

M. G. Imhof, 'Estimation of 3D Reservoir Heterogeneity using Seismic Heterogeneity Cubes', 64th Meeting in Florence, European Association of Geoscientists & Engineers, Extended Abstracts, 2002.

E. Nowak, M. G. Imhof, and W. Kempner, 'Object-Based Stochastic Facies Inversion: Application to the Characterization of Fluvial Reservoirs', 72nd Annual Internat. Mtg., Soc. Expl. Geophys., Expanded Abstracts, 2002.

K. L. Mize, 'Development of Three-Dimensional Geological Modeling Methods using Cores and Geophysical Logs, West Coalinga Field, California', MS Thesis, Clemson University, 2002.

M. G. Imhof, 'Scale Dependence of Reflection and Transmission Coefficients', *Geophysics*, in press.

M. G. Imhof and W. Kempner, 'Seismic Heterogeneity Cubes and Corresponding Equiprobable Simulations', *Journal of Seismic Exploration*, submitted.

HIGH-RESOLUTION DETERMINISTIC SEISMIC RESERVOIR CHARACTERIZATION

S. Mahapatra and M. G. Imhof, Virginia Tech

INTRODUCTION

The process of Reservoir Characterization is a three-dimensional quantitative determination of a reservoir, including its limits, structural framework, volume, heterogeneity, and corresponding distribution of rock and fluid properties, to maximize production and minimize costs.

The conventional seismic reservoir characterization involves integration of geologic and seismic data. The modeling is done with the help of lithological parameters, estimated from the well cuttings, core, and wireline data, but the estimation pertains to the well bore only. The inter-well gaps are filled either by geologic conceptual visualization or by applying geostatistical methods. In either case, the estimation of these key petrophysical parameters may be inconclusive and differ from reality.

3D seismic data provides an image of reservoir heterogeneity. The current state-of-the-art is volume visualization and geobody analysis. The major drawbacks are lithologic ambiguities, and yet too much detail for direct use in reservoir modeling. In this project, we intend to drive these approaches to their limit and investigate how to overcome these problems.

GEOLOGY

Coalinga anticline is one of a series of an echelon folds that modify the generally homoclinal eastern flank of the Diablo range along the west side of the San Joaquin Basin of California. The field is part of a Kreyenhagen-Temblor petroleum system that derives oil from organic-rich shales of Middle Eocene Kreyenhagen Formation. The Temblor Formation (Mid. Miocene sandstone) represents the inter play of shallow marine and non-marine depositional environments. The shallow unconsolidated sands of the Temblor formation are characterized as channel-cut sands, containing impermeable barriers. The Temblor formation is characterized by three different clastic subunits based on depositional environmental characteristics. The field is close to the San Andreas Fault and contains four unconformable surfaces (Basal Temblor, Button, Valv, and Top Temblor) representing incised-fill to sub-tidal depositional environments, which render the reservoir highly heterogeneous. In addition, cementation often masks original lithology and petrophysics.

The following facies groups were identified by our collaborators at Clemson University:

- Sands,
- Burrowed sands,
- Laminated sand,
- Silt and Clay,
- Fossiliferous Sand and Clay,
- Burrowed Clay,
- Limestone, and
- Calcareous cemented sediment.

PROCEDURE

The wireline logs (sonic and density) were correlated and the four unconformable surfaces identified based on the “base shale shifting” values. Aspect maps of these depth horizons were drawn to check the consistency in log correlation. The time equivalent of these unconformities were then transferred into the poststack 3D seismic data project and extended over the entire field.

DISCUSSION & CONCLUSION

The wire-log correlation and various aspect maps are attached (Fig. 2-8, 9-13). The strike of the area seems to be NNE-SSE. The highest structural relief is observed towards W-SW. The thickness of the Temblor formation is increasing downdip toward E with its maximum towards NNE. On the seismic data, offlap, reflector truncation, and onlap relationships are observed against the unconformities (Fig. 16-19). The 2-way time thickness of Temblor formation is about 240-260 ms; or 130-150, 30-40, and 35-40 ms for the three intervals bounded by the unconformities. As expected, the highest structural relief is observed towards W. The zone between Button and Basal Temblor contains a number of channel cuts (Fig. 14, 15, 17-19) which appear to be recut and restacked in the lower central part of the study area. This is most prominently observed in the strike direction. The depositional direction seems to be changing over the field as a function of geologic time of deposition. There is a mismatch when tracing reflector from N to S or vice versa. In addition, the Button and Valv surfaces appear to merge in the Western part indicating that portions of Button unconformity have been eroded by the overlaying Valv unconformity (Fig.17).

The exact geometry of these features is still being sorted out. Further data visualization and geobody analysis may help in delineating these bodies.

Seismic details

3-D survey carried out during 1996-2000 CDP Spacing 60 ft
2,263,483 seismic traces Both Prestack & poststack data

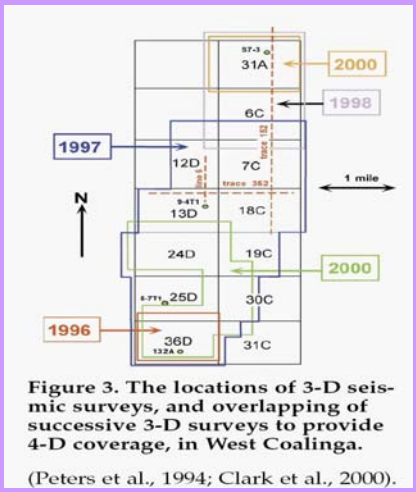

Figure 3. The locations of 3-D seismic surveys, and overlapping of successive 3-D surveys to provide 4-D coverage, in West Coalinga.

(Peters et al., 1994; Clark et al., 2000).

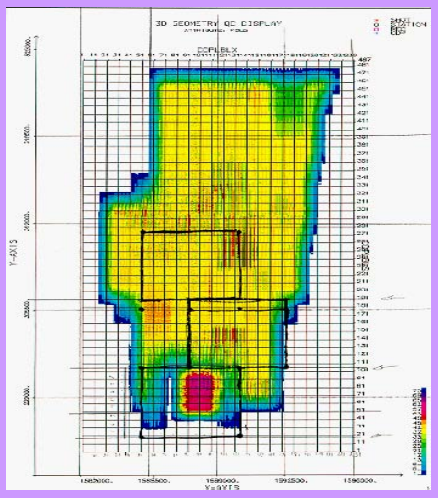

Figure 1

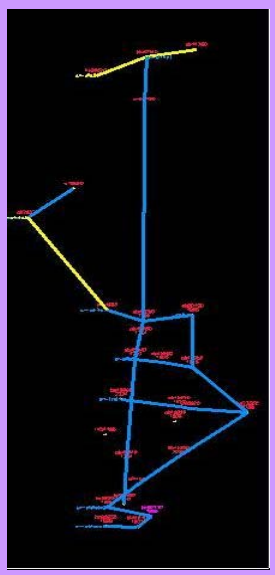

STUDY AREA SHOWING WELL LOCATIONS AND CROSS SECTION PROFILES

Figure 2

LOG CHARACTERISTICS OF WELL—be90220 SHOWING UNCONFORMITIES IN TEMBLOR FORMATION

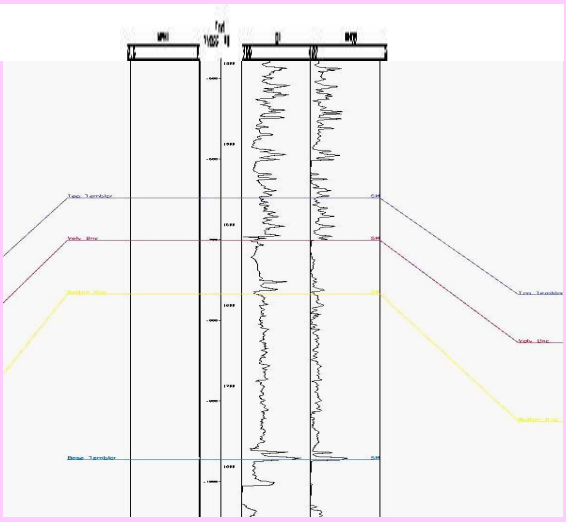

-- The unconformities are identified based on different Shale base lines

Figure 3

CORRELATION ALONG STRIKE

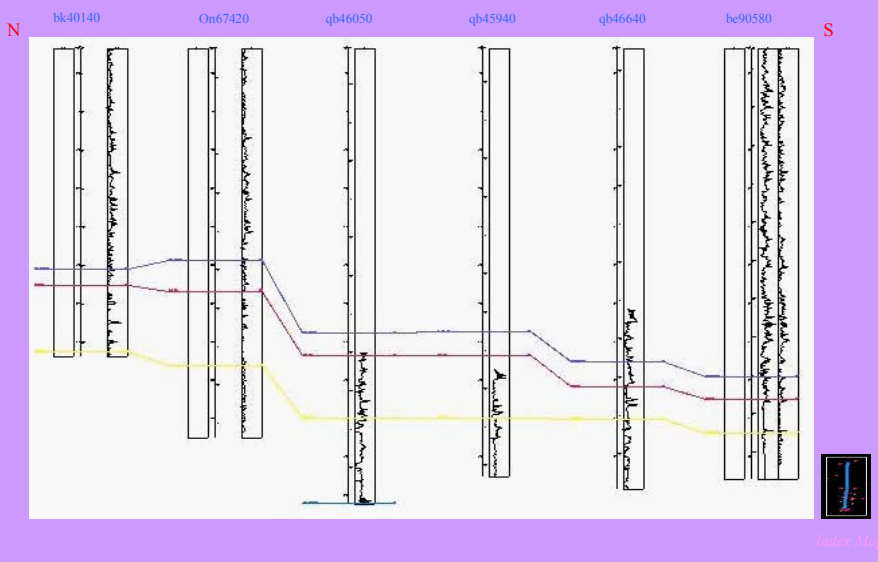

Figure 4

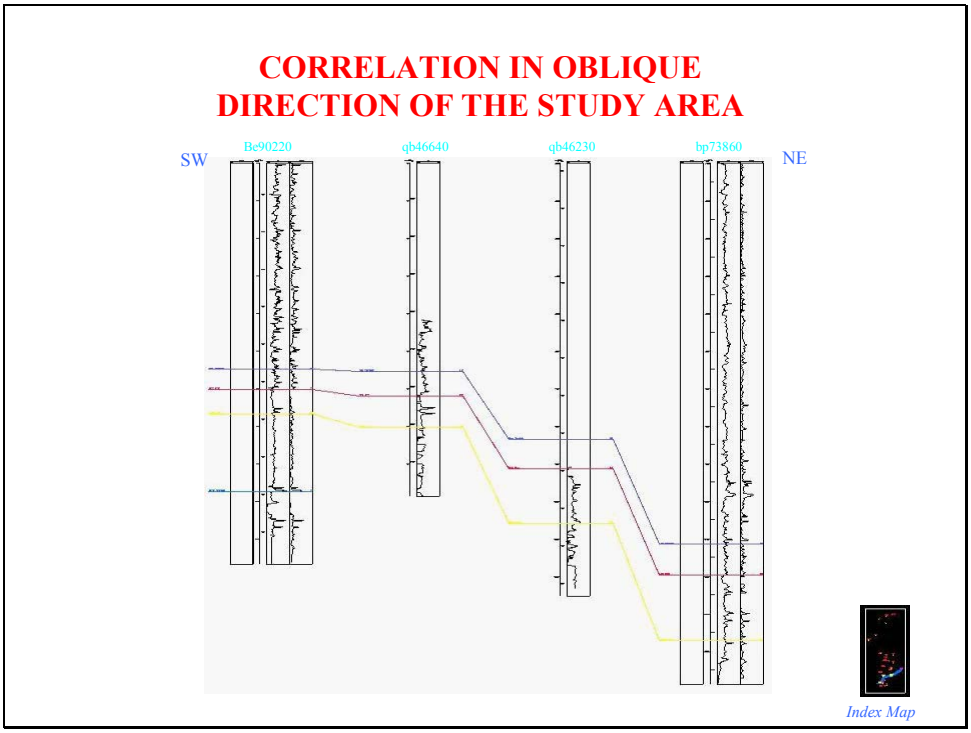

Figure 5

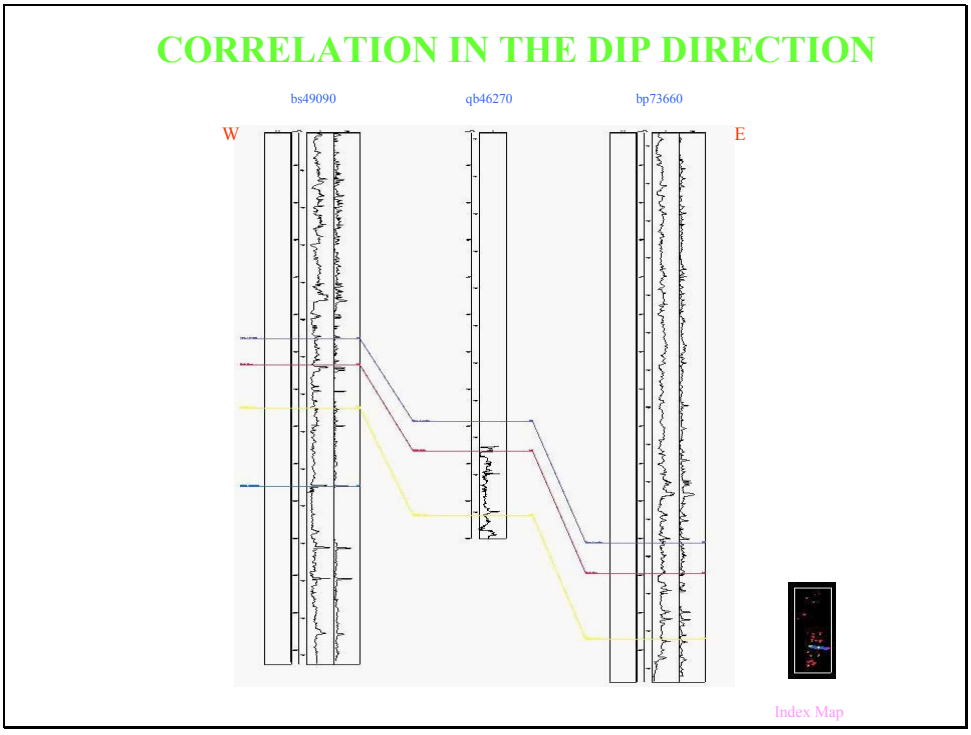

Figure 6

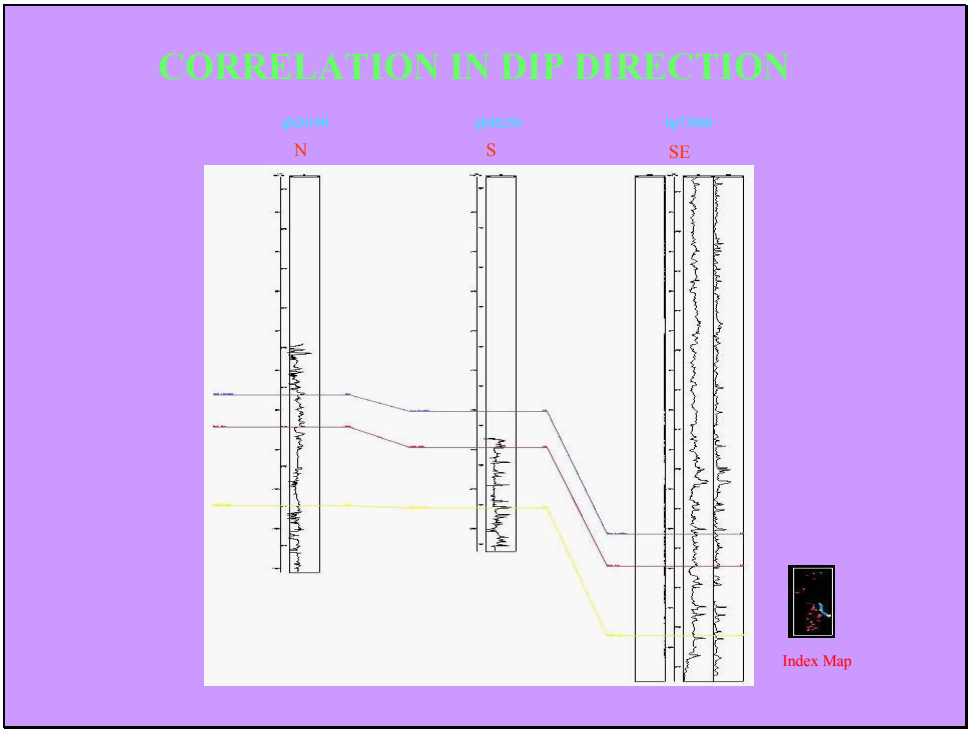

Figure 7

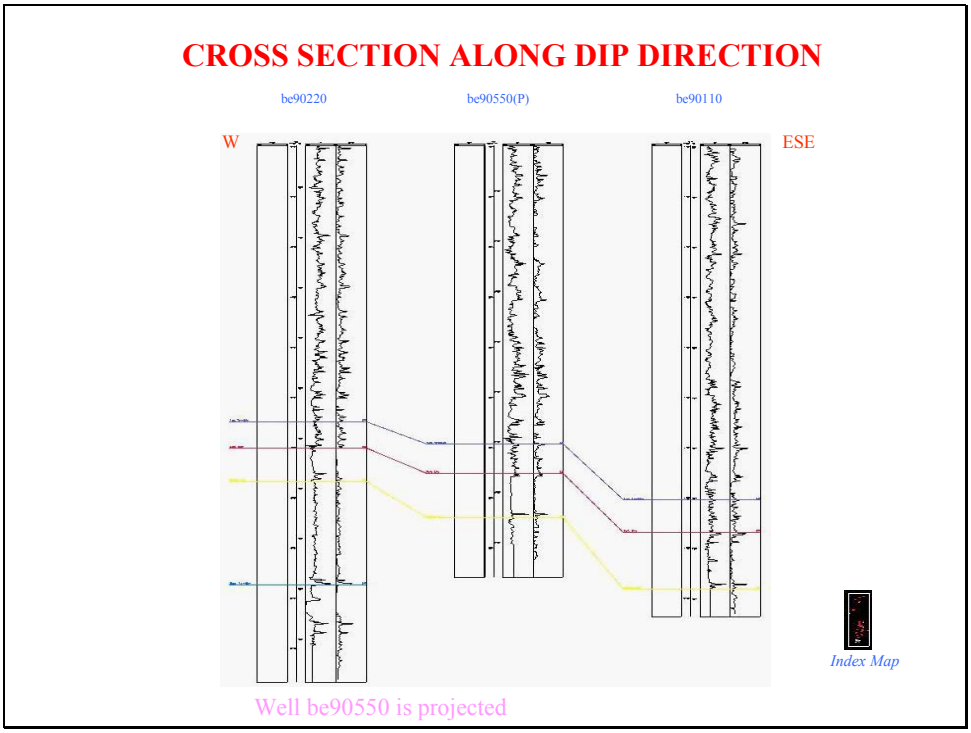

Figure 8

Depth Structure Contour Map on Top of Temblor Formation

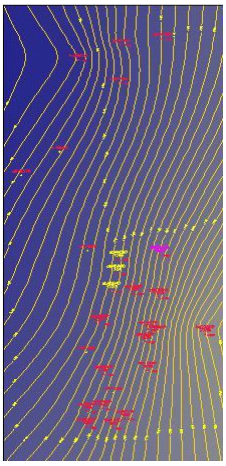

-Shows Strike NNE-SSW and dip towards E-SE
-The highest part is towards NW corner

Figure 9

Depth Structure Contour Map on Top of Valv Unconformity

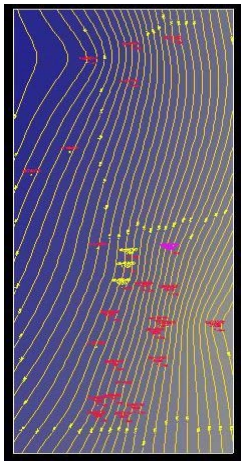

-Shows Strike NNE-SSW and dip towards E-SE
-The highest part is towards NW corner

Figure 10

Depth Structure Contour Map on Top of Button Unconformity

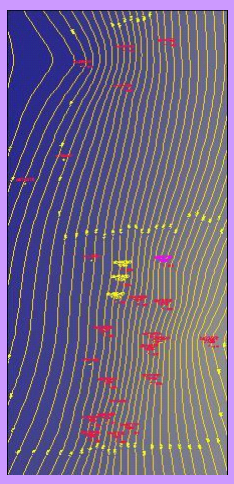

-Shows Strike NNE-SSW and dip towards E-SE
-The highest part is towards NW corner

Figure 11

Depth Structure Contour Map on Top of Base Temblor

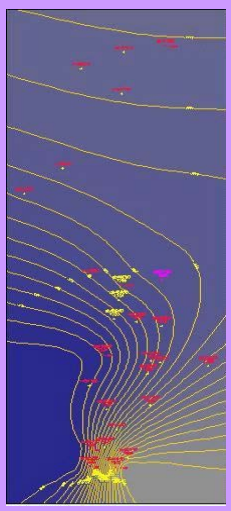

-The conspicuous contour merging in the bottom part is due to lack of sufficient well data

Figure 12

Isochore Map Between Top of Temblor And Top of Base Temblor

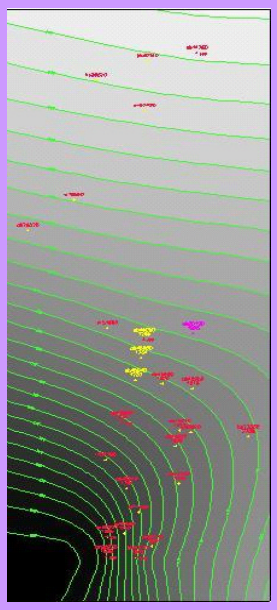

The thickness decreases towards SW suggesting higher depositional elevation.

Figure 13

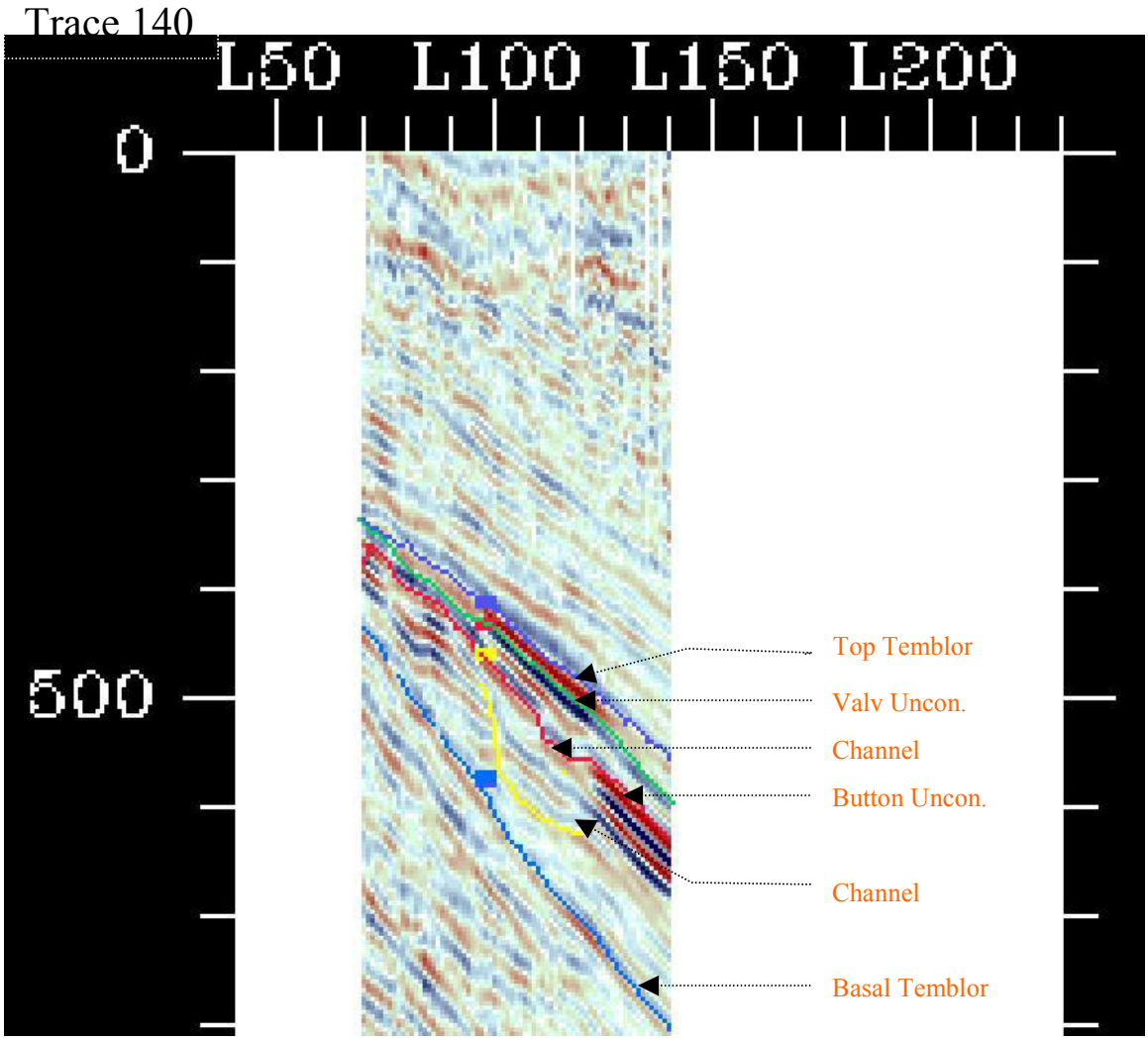
Trace 140
L50
L100
L150
L200
0
500
Top Temblor
Valv Uncon.
Channel
Button Uncon.
Channel
Basal Temblor

Figure 14

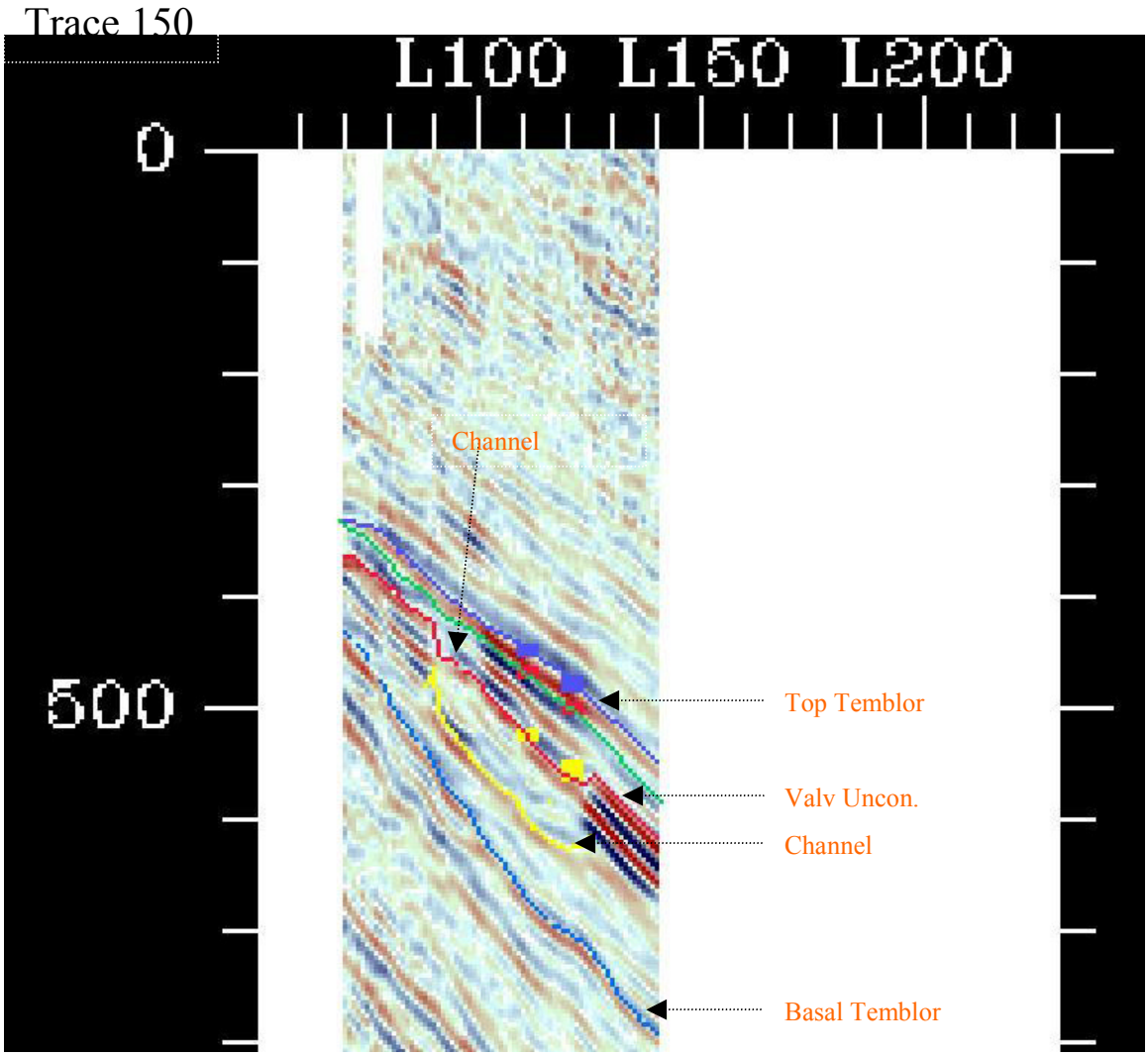
Trace 150
L100 L150 L200
0
500
Channel
Top Temblor
Valv Uncon.
Channel
Basal Temblor

Figure 15

Trace 255

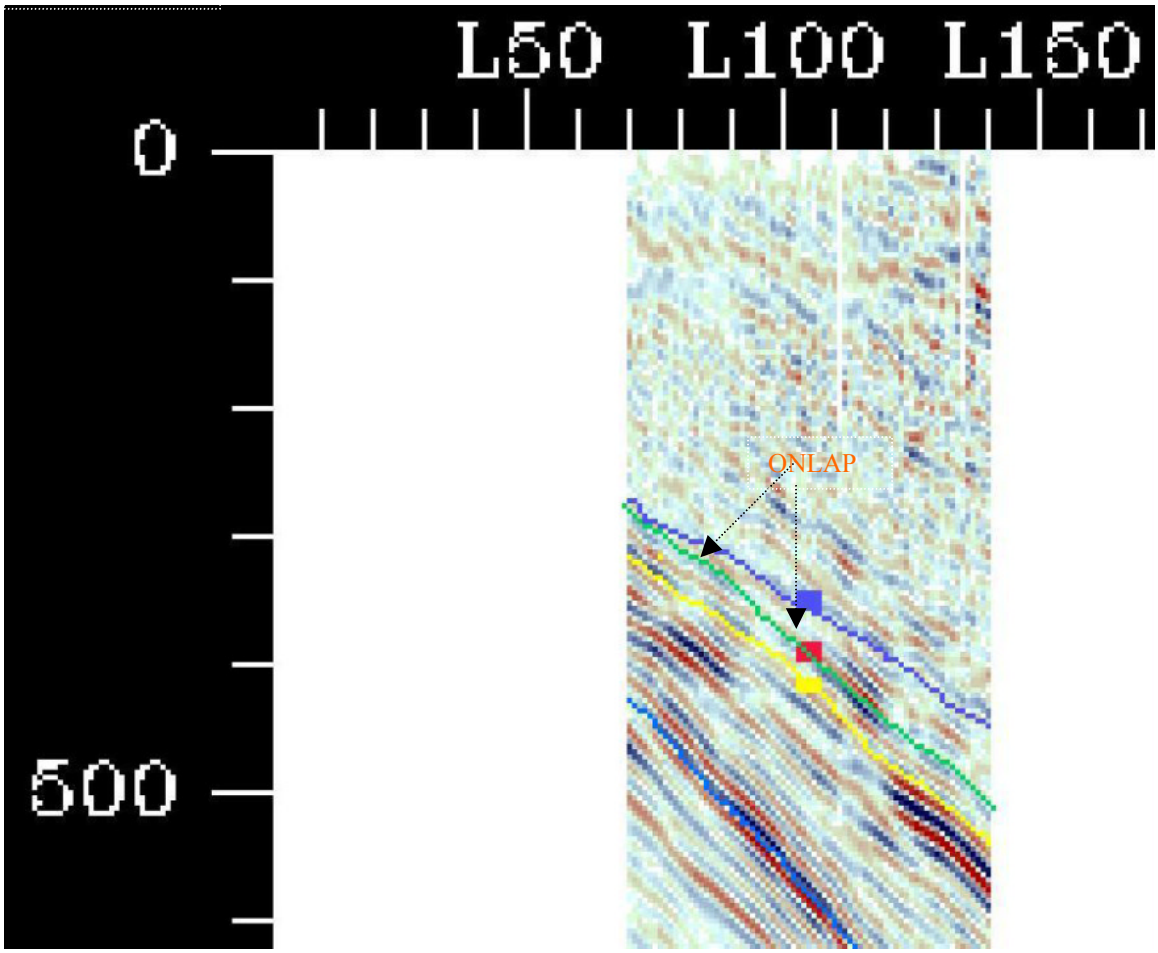

Figure 16

Line 110

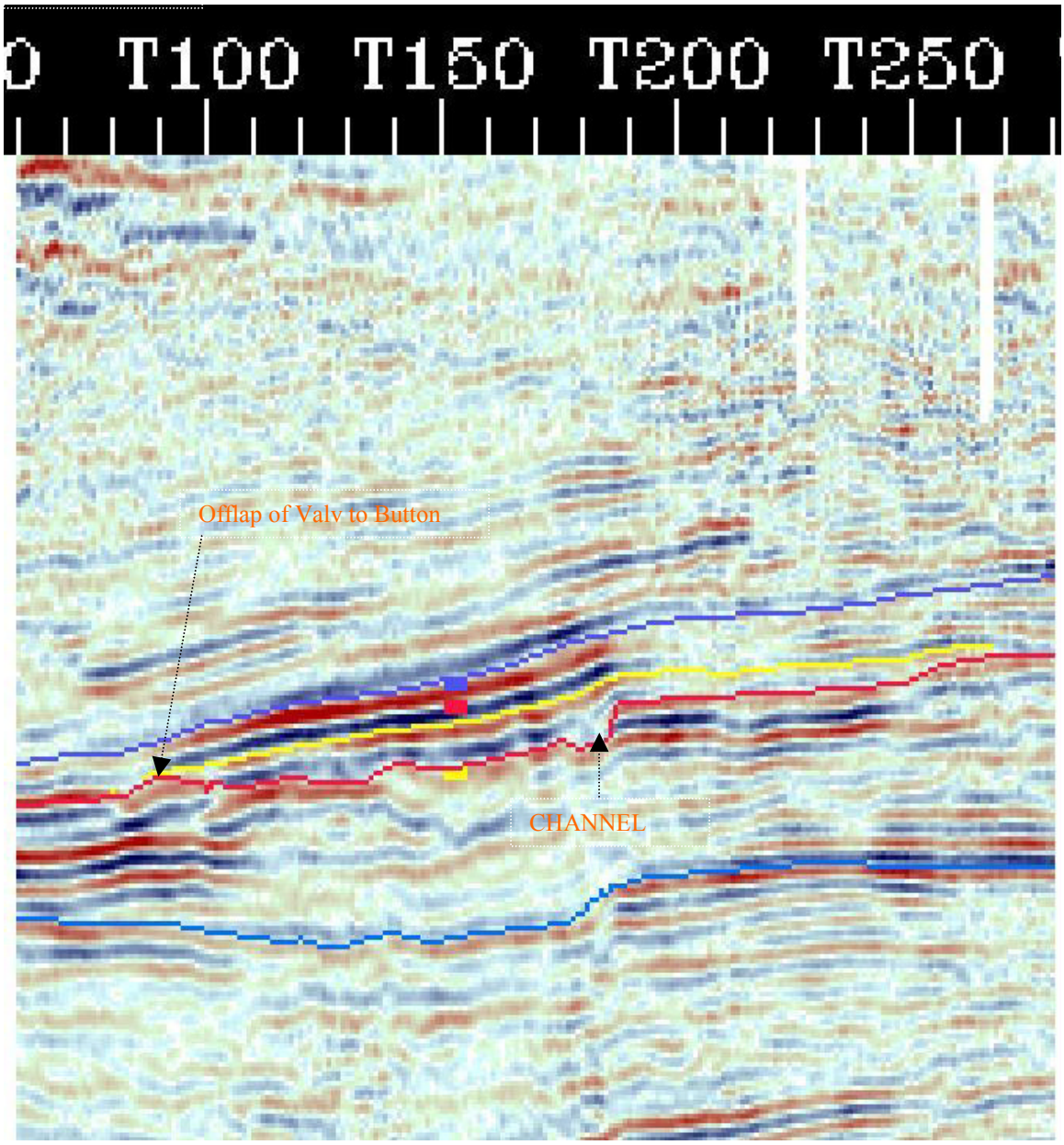

Figure 17

Line 120

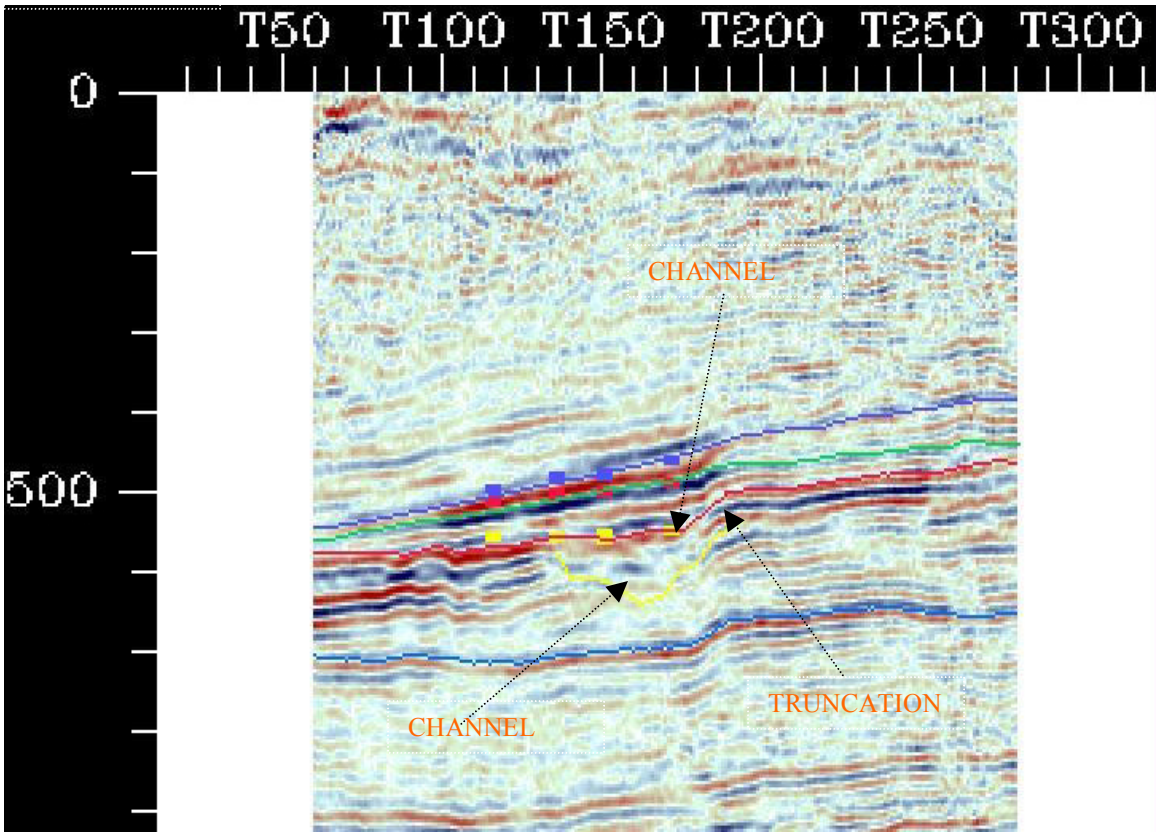

Figure 18

Trace 100

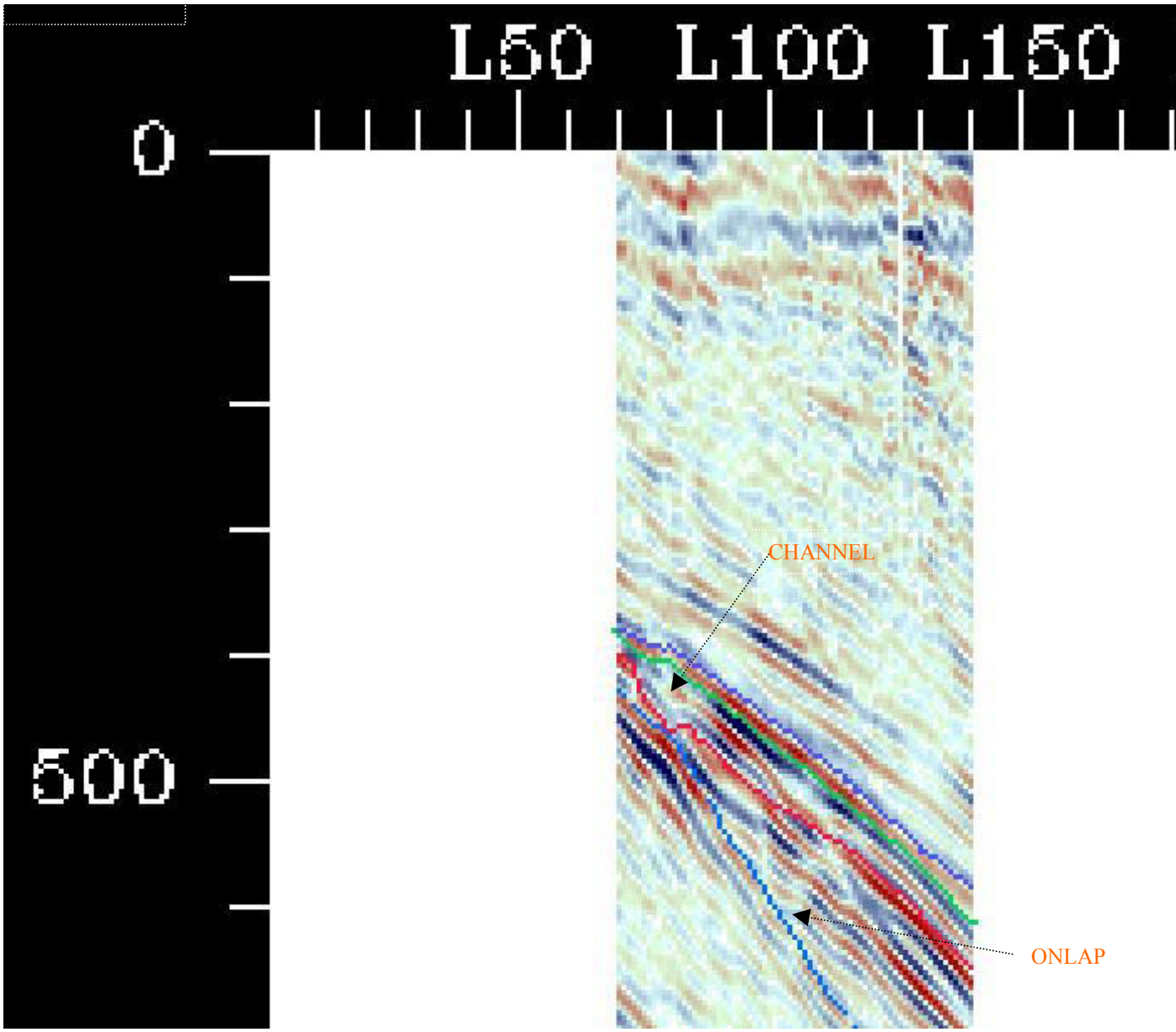

Figure 19

Seismic Heterogeneity Cubes and Corresponding Equiprobable Simulations

M. G. Imhof, Virginia Tech

ABSTRACT

Seismic heterogeneity cubes are attributes which measure local second-order statistics of seismic heterogeneity from 3-D datacubes. Seismic heterogeneity could relate to acquisition and processing footprints, structural features such as fracture or fault zones, or stratigraphic and lithologic heterogeneity. Acquisition and processing footprints may be removable with techniques currently being developed for the interpretation of similarity or amplitudes versus offsets (AVO).

Raw second-order statistics estimated from seismic data contain too many parameters to form useful seismic attributes. Instead, model statistics with only six parameters are fitted to the raw statistics. These six parameters contain three orthogonal correlation lengths and three orientations. From the stratigraphic viewpoint, the seismic heterogeneity could denote average dimensions and orientations of small sedimentary bodies, while the statistics might relate to average size, spacing, and orientations of fractures and joints for the structural point of view.

The six parameters are seismic attributes which can be visualized and directly used for interpretation. However, these attributes have a physical meaning because they can quantify local second-order statistics, for example of sedimentary bodies. One can perform geostatistical simulations using these parameters to obtain reservoir realizations which could be used for fluid flow modeling, risk analysis, etc. Commercial tools for geostatistical simulation are often based on the

assumption of stationarity, i.e., the statistics are invariant within a simulation volume. Heterogeneity cubes of different datasets show that this assumption is almost never justifiable. Hence, the convolutional approach of geostatistical simulation is modified to take advantage of the instationary statistics provided by the heterogeneity cubes. The resulting algorithm allows computation of reservoir realizations with spatially variant statistics.

INTRODUCTION

Imhof and Toksöz (2000) presented a method to estimate seismic heterogeneity from seismic data. This work has now been extended into a true 3-D seismic volume attribute which quantifies the heterogeneity contained in the seismic data. This heterogeneity is described by a spatial autocorrelation function. The parameters of these autocorrelation functions form the heterogeneity cubes.

Seismic heterogeneity could relate to acquisition and processing footprints or stratigraphic and lithologic heterogeneity. Clearly, the seismic heterogeneity could just be an artifact of the data acquisition or the data processing. These footprints, however, are also encountered at other steps of data processing (e.g., DMO and migration) and interpretation (e.g., similarity and other attributes). Many algorithms are currently introduced to remove systematic amplitude distortions caused by acquisition and processing (e.g., Marfurt et al., 1998; Canning and Gardner, 1998; Soubaras, 2002). The same methods might suppress or remove seismic footprint heterogeneity. Seismic heterogeneity could also be caused by stratigraphic or lithologic heterogenity. Each layer may contain numerous short-scale variations of the material properties if the layer is a composite of smaller sedimentary bodies. The seismic heterogeneity parameters may denote average dimensions and orientations of these bodies.

The heterogeneity parameters will be estimated at every point of interest of a seismic data volume. Typically, the seismic heterogeneity parameters will vary from point to point, but because the parameters quantify second-order statistics of the data, it follows that these statistics will be insta-

tionary. In addition to using the heterogeneity cubes as seismic attributes, they allow computation of stochastic realizations compatible with these instationary statistics described by the heterogeneity cubes by using instationary simulation algorithms. Many simulation tools, however, cannot handle instationary statistical models but only locally stationary ones, i.e., models composed of compact regions with different uniform statistics. Hence, the popular convolutional algorithm of geostatistical simulation (Frankel and Clayton, 1986; Kerner, 1992; Ikelle et al., 1993) is extended to allow use of instationary input parameters.

METHOD

Imhof and Toksöz (2000) presented a method to estimate seismic heterogeneity from seismic data. The method estimated one set of heterogeneity parameters from a large volume of data. In addition, the results were only pseudo three-dimensional because the algorithm operated on data slices instead of data volumes. Pseudo 3-D results could be obtained by applying the algorithm on orthogonal slices of data (Imhof, 2001). This procedure was prone to yield inconsistent results. In addition, only a very limited amount of data was used which forced the use of large data windows to obtain reliable heterogeneity estimates. The result was spatial averaging and smearing which limited the usefulness of the estimates. In this contribution, the algorithm is extended to yield truly 3-D seismic volume attributes which are not hampered by these problems.

Estimation

The heterogeneity attributes are calculated at every point (x, y, z) of a seismic poststack datacube d. A little probe volume v, centered at the current (x, y, z), is extracted from the full datacube d. This probe v is then crosscorrelated with the datacube d to estimate the local crossvariance function $\hat{\rho}(\Delta x, \Delta y, \Delta z; x, y, z)$ at point (x, y, z) for a number of different correlation lags Δx, Δy,

and Δz.

$$\hat{\rho}(\Delta x, \Delta y, \Delta z; x, y, z) = \frac{1}{N(\Delta x, \Delta y, \Delta z)} \times \sum_{\substack{(\delta x, \delta y, \delta z) \\ \in \\ V(x,y,z)}} v(x+\delta x, y+\delta y, z+\delta z) \cdot d(x+\delta x+\Delta x, y+\delta y+\Delta y, z+\delta z+\Delta z) \quad (1)$$

The factor $N(\Delta x, \Delta y, \Delta z)$ normalizes the result with the number of terms used in the summation (1). The averaging or summation volume $V(x, y, z)$ for the current center point (x, y, z) is arbitrary. Large volumes V provide more reliable statistics, but at the price of potentially averaging instationary data. Small volumes reduce the effect of lumping instationary data, but they degrade the resulting statistics due to the smaller amount of data used in the estimation. As a compromise, we often use $V(x, y, z) = v(x, y, z)$, i.e., the summation volume V equals the probe v. The local crossvariance $\hat{\rho}$ is normalized to unity for $\Delta x = \Delta y = \Delta z = 0$ which yields the local crosscorrelation function $(LCCF)$ $\hat{R}(\Delta x, \Delta y, \Delta z; x, y, z)$:

$$\hat{R}(\Delta x, \Delta y, \Delta z; x, y, z) = \frac{\hat{\rho}(\Delta x, \Delta y, \Delta z; x, y, z)}{\hat{\rho}(0, 0, 0; x, y, z)} \quad (2)$$

The $LCCF$ $\hat{R}(\Delta x, \Delta y, \Delta z; x, y, z)$, however, contains too many values to be of direct use, even if it is computed for only a few lags. To be useful as seismic attributes, the number of values needs to be reduced. Instead of directly using the raw estimate $\hat{R}$ of the $LCCF$, the number of parameters is decimated by fitting the estimate $\hat{R}$ with a model $LCCF$ $\bar{R}$ which contains only six free parameters. This reduction not only makes the $LCCF$ more manageable, but also improves the statistics because less parameters are estimated with the same data volumes V and v.

Presently, the model $LCCF$ $\bar{R}$ is an anisotropic Gaussian function which allows rapid calculation of $LCCF$ models and equiprobable realizations. The method does not depend on this choice of model $LCCF$, though. Any other 3-D autocorrelation function (or the related variogram) could be used (e.g., Lantuéjoul, 2002). Each direction is scaled independently with a characteristic scale,

the correlation length. The three orthogonal correlation lengths are ordered by size: $a > b > c$.

$$\bar{R}(\Delta x, \Delta y, \Delta z; a, b, c, \phi_x, \phi_y, \phi_z) = \exp\left(-u^2/a^2 - v^2/b^2 - w^2/c^2\right) . \tag{3}$$

For greater flexibility, the model *LCCF* $\bar{R}$ is rotated with the Euler angles ϕ_x, ϕ_y, and ϕ_z around the Cartesian x, y, and z axes. The parameters (u, v, w) are obtained from the lags $(\Delta x, \Delta y, \Delta z)$ by rotation with the rotation matrix $\mathbf{S}(\phi_z, \phi_y, \phi_x)$ (e.g., Schwarz, 1989).

$$\begin{pmatrix} u \\ v \\ w \end{pmatrix} = \mathbf{S}(\phi_z, \phi_y, \phi_x) \cdot \begin{pmatrix} \Delta x \\ \Delta y \\ \Delta z \end{pmatrix} \tag{4}$$

$$\mathbf{S} = \begin{pmatrix} \cos\phi_y \cos\phi_z & -\cos\phi_y \sin\phi_z & -\sin\phi_y \\ -\sin\phi_x \sin\phi_y \cos\phi_z + \cos\phi_x \sin\phi_z & \sin\phi_x \sin\phi_y \sin\phi_z + \cos\phi_x \cos\phi_z & -\sin\phi_x \cos\phi_z \\ \cos\phi_x \sin\phi_y \cos\phi_z + \sin\phi_x \sin\phi_z & -\cos\phi_x \sin\phi_y \sin\phi_z + \sin\phi_x \cos\phi_z & cos\phi_x \cos\phi_y \end{pmatrix} \tag{5}$$

The angle ϕ_z denotes the dip orientation (or yaw) of the largest correlation length a, i.e., the direction of maximal continuity. The orientation is limited to the range $0 \leq \phi_z < 360°$. The angle $0 \leq \phi_y < 90°$ specifies the dip (or pitch) of the *LCCF* at the direction of maximal continuity. Finally, the tilt (or roll) ϕ_x indicates how much the *LCCF* has been rotated around the direction of maximal continuity. The tilt angle is confined to the range of $-90 < \phi_x < +90°$. The orientation ambiguity is resolved by defining the orientation with the downward dip direction. Figure 1 illustrates these angles for the isosurface $\bar{R} = 1/e$ for the characteristic lengths $a = 5$, $b = 2.5$, and $c = 0.75$.

The optimal set of parameters $(a, b, c, \phi_x, \phi_y, \phi_z)$ minimizes the root-mean-square (RMS) difference ϵ between the model *LCCF* $\bar{R}(\Delta x, \Delta y, \Delta z)$ and the data *LCCF* $\hat{R}(\Delta x, \Delta y, \Delta z)$.

$$\epsilon^2 = \sum_{\Delta x, \Delta y, \Delta z} \left(\hat{R}(\Delta x, \Delta y, \Delta z; x, y, z) - \bar{R}(\Delta x, \Delta y, \Delta z; a, b, c, \phi_x, \phi_y, \phi_z)\right)^2 \tag{6}$$

By repeating averaging and optimization at every point (x, y, z) of the dataset, one obtains the

heterogeneity cubes for the characteristic lengths a, b, and c, the orientation angles ϕ_x, ϕ_y, and ϕ_z, and the minimization error ϵ^2. The original scheme (Imhof and Toksöz, 2000) determined the optimal set of parameters by systematic search. In three dimensions, however, systematic search is impractical. Either the parameters are resolved too coarsely, or the number of cases to examine becomes enormous. If only ten cases are examined for each parameter, then one million cases need to the tested for every point of the dataset! As a more practical alternative, we use a nonlinear optimization algorithm which allows placing bounds on the parameters (Zhu et al., 1997). For example, the orientation ϕ_z is periodic and bound between 0 and 360°, or the correlation lengths a, b, and c are ordered by size $a > b > c$.

The main problems with nonlinear optimization are non-convergence and trapping in local minima. Because the optimal set of parameters is not only estimated at one point but in the entire data volume, suboptimal estimates can be identified as outliers by visual or automatic inspection. Suboptimal estimates can be removed by, for example, (periodic) median filtering.

Simulation

Random realizations $m(\mathbf{x})$ with a prescribed autocorrelation function (ACF) are often computed using a convolutional model (Frankel and Clayton, 1986; Kerner, 1992; Ikelle et al., 1993). The powerspectrum $S(\mathbf{k})$ is the spatial Fourier transform of the autocorrelation $R(\mathbf{x})$.

$$S(\mathbf{k}) = \frac{1}{(2\pi)^3} \iiint R(\mathbf{x}) e^{-i\mathbf{k}\cdot\mathbf{x}} \, d\mathbf{x} \tag{7}$$

All models with this ACF R have the same amplitude spectrum $A(\mathbf{k}) = \sqrt{S(\mathbf{k})}$. The differences between these models are their phase spectra. Random realizations $r(\mathbf{x})$ can be simulated by inverse Fourier transformation back to the space domain of the amplitude spectrum $A(\mathbf{k})$ with randomized phase spectra.

$$r(\mathbf{x}) = \iiint A(\mathbf{x}) e^{2\pi i \; uniform[0,1]} e^{i\mathbf{k}\cdot\mathbf{x}} \, d\mathbf{k} \tag{8}$$

If the zero-phase realization $r_0(\mathbf{x})$ is computable analytically, one can also convolve $r_0(\mathbf{x})$ with a realization of white noise $n(\mathbf{x})$:

$$r(\mathbf{x})_{stationary} = r_0(\mathbf{x}) * n(\mathbf{x}) \tag{9}$$

with

$$r_0(\mathbf{x}) \equiv \iiint A(\mathbf{x}) e^{i\mathbf{k}\cdot\mathbf{x}}\, d\mathbf{k} \tag{10}$$

and

$$n(\mathbf{x}) \equiv \iiint e^{2\pi i\ uniform[0,1]} e^{i\mathbf{k}\cdot\mathbf{x}}\, d\mathbf{k}\,. \tag{11}$$

The Fourier approach (8) is typically much faster than convolution in the space domain (11).

The autocorrelation described by the heterogeneity cubes, however, varies spatially. To compute realizations based on the heterogeneity cubes, the convolutional approach is modified:

$$r(\mathbf{x})_{instationary} = r_x\Big(a(\mathbf{x}), b(\mathbf{x}), c(\mathbf{x}), \phi_x(\mathbf{x}), \phi_y(\mathbf{x}), \phi_z(\mathbf{x}); \mathbf{x}'\Big) * n(\mathbf{x}')\Big|_{\mathbf{x}=\mathbf{x}'} \tag{12}$$

The same white noise field $n(\mathbf{x}')$ is used to compute the realization $r_{instationary}(\mathbf{x})$ at every point. For every point $\mathbf{x}$, however, the zero-phase realization r_x, which is compatible with the heterogeneity parameters at this point, is used in the convolution with the white noise. The convolution coordinate $\mathbf{x}'$ has been tagged to distinguish it clearly from the current point $\mathbf{x}$ where a numerical value of the realization is computed. The convolution (12) is evaluated only at the current point $\mathbf{x}$. The Fourier approach (8) could also be modified to compute these instationary realizations. However, the inverse Fourier transformation needs to be performed for every point anew because the heterogeneity parameters, and hence the Fourier kernel, differ. The entire realization with the exception of the current point $\mathbf{x}$ will be discarded, which makes the convolutional approach (12) more efficient when the zero-phase realization r_0 can be calculated analytically. For our Gaussian model *LCCF* (3), the analytical zero-phase realization is:

$$r_x(x, y, z; a, b, c, \phi_x, \phi_y, \phi_z) = \sqrt{\frac{8}{a\ b\ c\ \pi^3}}\ e^{-2(u^2/a^2 + v^2/b^2 + w^2/c^2)}\,, \tag{13}$$

where the parameters u, v, and w are obtained by rotation (5) of x, y, and z.

EXAMPLE

The example is from the giant Coalinga oil field in the San Joaquin Valley in California (Figure 2). The Coalinga field parallels the upturned, monoclinal west margin of the San Joaquin basin. Clark et al. (2001) presented the 3-D seismic dataset used in this contribution and discussed the extremely complex subsurface stratigraphy in detail. For completeness, some key data are repeated here.

Lower to Middle Miocene strata are prolific hydrocarbon reservoirs in several San Joaquin Valley oil fields. One of the largest fields, Coalinga, has produced 850 million barrels of oil since 1887. Currently, 90% of the production is from nearshore to nonmarine, Middle Miocene sandstones of the Temblor Formation at depths of $500 - 4500$ ft. Porosity averages 34% and permeability is $20 - 4000$ md. The maximum thickness of the Temblor is around 700 ft. Wide variations in oil gravity and complex stratigraphy result in most wells producing only a few barrels per day of heavy crude ($10 - 12\,^{\circ}$API gravity). To enhance recovery, steam is injected to reduce viscosity and drive the oil toward production wells.

The lower Temblor sequence in the subsurface contains numerous thin ($5 - 10$ ft) and discontinuous sandstones which are interpreted as tidal channels that truncate sandy to muddy tidal flat facies. Onlap relations and mixed nonmarine and tide-dominated nearshore facies in outcrop indicate estuarine deposition. Although the tidal channel sandstones tend to be laterally discontinuous and interbedded with lower-permeability sandstones and impermeable mudstones, stacked tidal channel sandstones in a few wells create thick ($20 - 30$ ft), amalgamated, high-permeability reservoirs with high oil saturations. The stacked reservoirs of the lower Temblor are characterized by discontinuous positive amplitudes, which onlap the basal Temblor unconformity.

The middle Temblor sequence contains thick ($50 - 100$ ft), laterally continuous, coarsening-upward sandstones that represent prograding units deposited along a wave- and tide-influenced shoreline

with a north-south trend in a deeper marine setting than the basal sequence. Permeabilities and oil saturations tend to be higher than in the lower Temblor. The middle Temblor is characterized by continuous positive amplitude reflections which onlap the Buttonbed unconformity and truncate the basal Temblor sequence.

The upper Temblor contains stacks of thin, laterally continuous, and coarsening-upward sandstones with carbonate cement. They are interpreted as prograding shoreline deposits, oriented with a north-south trend, which represent a slightly deeper marine setting than the middle sequence with less tidal influence. Heavy cementation can obscure all sedimentary structures. Despite cementation, permeability and saturation are large enough to form economic pools. The upper Temblor is characterized by fairly continuous positive amplitude reflections, which onlap the Valv unconformity. In summary, the Temblor sequences contain rapid facies changes in vertical and lateral directions which are overprinted by cementation and multiple unconformities with complex onlap and truncation geometries.

Figure 3 presents a subset of the seismic datacube for a focus area with 221 inlines and 71 crosslines. Each CDP box is 60×60 ft (20×20 m) with a temporal sampling interval of 4 ms. The top Temblor horizon at 400 ms has been used to flatten the dataset. The Temblor formations consist of the strong amplitude events below 400 ms with a thickness of up to 200 ms. In this study, we will concentrate on a timeslice at 440 ms, or 40 ms below the top Temblor horizon. At this depth, we expect the upward-coarsening sand bars of the middle Temblor with north-south orientation deposited in a subtidal environment. Figure 4 presents seismic amplitude, instantaneous amplitude, instantaneous frequency, and similarity. Bright instantaneous amplitudes correlate with high similarities and reduced instantaneous frequencies. The effect could be caused by steam which often increases amplitudes by increasing impedance contrasts (Tague et al., 1999). Steam can also reduce instantaneous frequencies by attenuation (Hedlin et al., 2001). Lower frequencies may increase similarity because shifts in phase or time have a lesser effect on the wavelet. The figures also show a distinct difference between the northern (upper) and southern (lower) halfs of the area. The northern part exhibits higher instantaneous frequencies, lower instantaneous amplitudes, and lower similarities than the southern part.

Figure 5 presents slices through the heterogeneity cubes for the long correlation parameter a at 440 ms as functions of probe volume size. Four different probe volumes were tested: $5 \times 5 \times 5$, $9 \times 9 \times 9$, $13 \times 13 \times 13$, and $17 \times 17 \times 17$. Small volumes may provide better localized statistical estimates, but are also based on less data which increases estimation errors. Furthermore, long correlation lengths are ill-constrained by small probe volumes. Large volumes average over more data which provides more reliable estimates, but may mix different statistical facies which might render the estimates ambiguous and decrease prognostic power. Furthermore, we found that large volumes tend to bias the estimates toward shorter correlation lengths. Independent of probe-volume size, we find that the northern half is basically bimodal with correlation lengths around 5 and 40 cdp. Small volumes yield predominantly 40 cdp correlations, while large volumes yield more short, 5 cdp correlations. The southern half contains a broad variety of correlation lengths which often fluctuate rapidly. One recognizes a trend of long correlation lengths which blurs with increasing size of the probe volume. Numerical experiments indicate that the vertical dimension of the probe volume has a stronger effect on the estimation results than the lateral dimensions. The number of time samples predominantly affects spatial patterns, while the number of spatial samples relates to smoothing, and hence, pattern continuity. Nevertheless, the similarity slice of Figure 4(b) and the heterogeneity slices of Figure 5 for the long-correlation length a correlate to large degrees.

Figure 6 shows the intermediate correlation length b and the angles of orientation, dip, and tilt for a probe volume of $9 \times 9 \times 9$ samples. The intermediate correlation length b basically mimics the long-range estimates a, but with shorter correlation lengths. Heterogeneity is mostly oriented in the north-south direction with minor dips and tilts. Large tilts often appear to be edge effects caused by an incomplete distribution of correlation lags. Since the seismic dataset has only been time migrated, dip and tilt are pseudo angles and would need to be mapped to real angles.

The short correlation length c is not shown because it is fairly constant around $1.5\Delta t$. Data processing, especially deconvolution, tends to reduce the vertical or temporal autocorrelation function toward a spike. All heterogeneity attributes are only presented as time or horizon slices, although they are true volume attributes. But their rapid variation in the vertical direction makes recogni-

tion of patterns very difficult. In addition, interpretation of orientation, dip, and tilt from cross sections is typically more difficult than from map views (Imhof, 2001).

Finally, Figure 7 presents four equiprobable realizations based on the estimated heterogeneity cubes a, b, c, ϕ_x, ϕ_y, and ϕ_z. To ease comparison with the heterogeneity cubes presented in Figures 5 and 6, the realizations are shown as slices at 440 ms depth, or 40 ms below Top Temblor. Each realization is an instationary random field with zero mean and unit variance which yields stochastic volumes with values roughly between -3 and 3 which could be interpreted as some kind of normalized impedance. All realizations were simulated using algorithm (12). Their only differences are the initial white-noise volumes passed through the instationary filter. Comparison of the realizations 7 and the heterogeneity cubes 5 and 6 shows that the simulated heterogeneity follows the orientations prescribed by the heterogeneity orientation ϕ_z. Similarly, long correlation lengths coincide with smoother realizations. As one may expect, the realizations in the northern and southern halves of the study area are rather different. In the northern half, we find long-scale heterogeneity with predominant north-south orientation. In the southern half, we obtain mixtures of long and short-scale heterogeneity with more directional variability which allows nonlinear connectivity over large areas.

DISCUSSION AND CONCLUSIONS

We presented an algorithm for estimating instationary second-order statistics from seismic data, which we termed seismic heterogeneity cubes because these statistics attempt to quantify 3-D seismic heterogeneity. The seismic heterogeneity could either relate to structure, stratigraphy and lithology, or acquisition and processing. For the present example, we believe that the seismic heterogeneity is caused by lithologic heterogeneity because we attempted to remove gross structure by flattening the data on the Top Temblor horizon. Fractures and faults could result in seismic heterogeneity, but neither fractures nor faults have been reported in the study area. Our results may be biased by acquisition and processing footprints as we did not attempt to remove such artifacts. Algorithms for footprint removal are currently developed for a range of other seismic

applications and could be used to precondition the data before estimating seismic heterogeneity (e.g. Marfurt et al., 1998; Canning and Gardner, 1998; Soubaras, 2002). We believe that for our dataset from Coalinga field, acquisition or processing footprints are secondary to stratigraphic and lithologic heterogeneity because we did not detect obvious footprints on either amplitudes or on other seismic attributes.

We attempt to estimate instationary statistics from seismic data. Ideally, one would derive these statistics from ensemble averages, i.e., by averaging over different realizations of the reservoir. Obviously, ensemble averaging is impractical because only one Coalinga field exists. Hence, we have to substitute spatial averages for ensemble averages which imposes a tradeoff between reliability and spatial contamination (or resolution). Using a small seismic data volume to estimate local correlation minimizes spatial contamination, but yields large estimation errors which cause increased spatial variability of the statistical estimates. Furthermore, long correlation lengths are ill-constrained by small probe volumes and short correlation lags which increases estimation errors for long correlation lengths. Unfortunately, larger volumes increase the likelihood of mixing different statistical facies which, in the limit, may render the resulting statistics meaningless. We observed that larger volumes are biased toward shorter correlation lengths. We also found that extending the probe volume in time or depth has a great effect on the resulting patterns of correlation parameters. Increasing the spatial size of the probe volume causes smearing and smoothing of the correlation patterns which increases the pattern continuity. In the presented example, we compromised with a probe volume of $9 \times 9 \times 9$ samples ($32\,\text{ms} \times 480\,\text{ft} \times 480\,\text{ft}$, or $32\,\text{ms} \times 160\,\text{m} \times 160\,\text{m}$). The temporal probe extent of 32 ms is similar to the observed seismic wavelet with its bandwidth of $10 - 60\,\text{Hz}$.

In the Coalinga field, we observed that second-order statistics are highly variable within the study area of $13,200 \times 4,200\,\text{ft}$ (or $4,400 \times 1,400\,\text{m}$). Clearly, the common assumption of stationary statistics is invalid not only for the entire field, but even within smaller patches. Unfortunately, commercially available technology for geostatistical simulation is often also based on the assumption of stationarity. To take advantage of our estimates of instationary statistics, we adapted the convolution based simulation method by using instationary filters to compute instationary realizations.

These realizations are equiprobable which allows exploration of their variations, commonalities, and differences to better understand risks and opportunities. In a future step, we will attempt to condition the instationary realizations to wireline and seismic data to obtain not just possible realizations, but optimal realizations which are compatible with all available data.

REFERENCES

A. Canning and G. H. F. Gardner. Reducing 3-D acquisition footprint for 3-D DMO and 3-D prestack migration. *Geophysics*, 63(4):1177–1183, 1998.

M. S. Clark, L. F. Klonsky, and K. E. Tucker. Geologic study and multiple 3-D surveys give clues to complex reservoir architecture of giant Coalinga oil field, San Joaquin Valley, California. *The Leading Edge*, 20(7):744–751, 2001.

A. Frankel and R. Clayton. Finite difference simulations of seismic scattering: implications for the propagation of short-period seismic waves in the crust and models of crustal heterogeneity. *J. Geophys. Res.*, B 91(6):6465–6488, May 1986.

K. Hedlin, L. Mewhort, and G. Margrave. Delineation of steam flood using seismic attenuation. In *71st Ann. Internat. Mtg., Soc. Expl. Geophys., Expanded Abstracts*, pages 1572–1575, 2001.

L. T. Ikelle, S. K. Yung, and F. Daube. 2-D random media with ellipsoidal autocorrelation functions. *Geophysics*, 58(9):1359–1372, 1993.

M. G. Imhof. The heterogeneity cube, a new family of seismic attributes. In *71st Ann. Internat. Mtg., Soc. Expl. Geophys., Expanded Abstracts*, pages 1548–1551, 2001.

M. G. Imhof and M. N. Toksöz. Estimation of stratigraphic heterogeneity using seismic reflection data. *J. Seis. Expl.*, 9(1), 2000.

C. Kerner. Anisotropy in sedimentary rocks modeled as random media. *Geophysics*, 57(4):564–576, 1992.

C. Lantuéjoul. *Geostatistical Simulation: Models and Algorithms*. Springer, Berlin, 2002.

K. J. Marfurt, R. M. Scheet, J. A. Sharp, and M. G. Harper. Suppression of the acquisition footprint for seismic sequence attribute mapping. *Geophysics*, 63(3):1024–1035, 1998.

H. R. Schwarz. *Numerical Analysis*. Wiley, New York, 1989.

R. Soubaras. Attenuation of acquisition footprint for non-orthogonal 3D geometries. In *64th Mtg. Eur. Assoc. Geosci. and Eng., Extended Abstracts*, 2002.

J. R. Tague, E. L. Von Dohlen, and G. F. Hollman. Optimizing steamflood performance using 3-D/4-D seismic imaging. *Petroleum Engineer International*, 72(6):29–34, June 1999.

C. Zhu, R. H. Byrd, P. Lu, and J. Nocedal. ALGORITHM 778: L-BFGS-B: Fortran subroutines for large-scale bound-constrained optimization. *ACM Trans. Math. Software*, 23(4):550–560, December 1997.

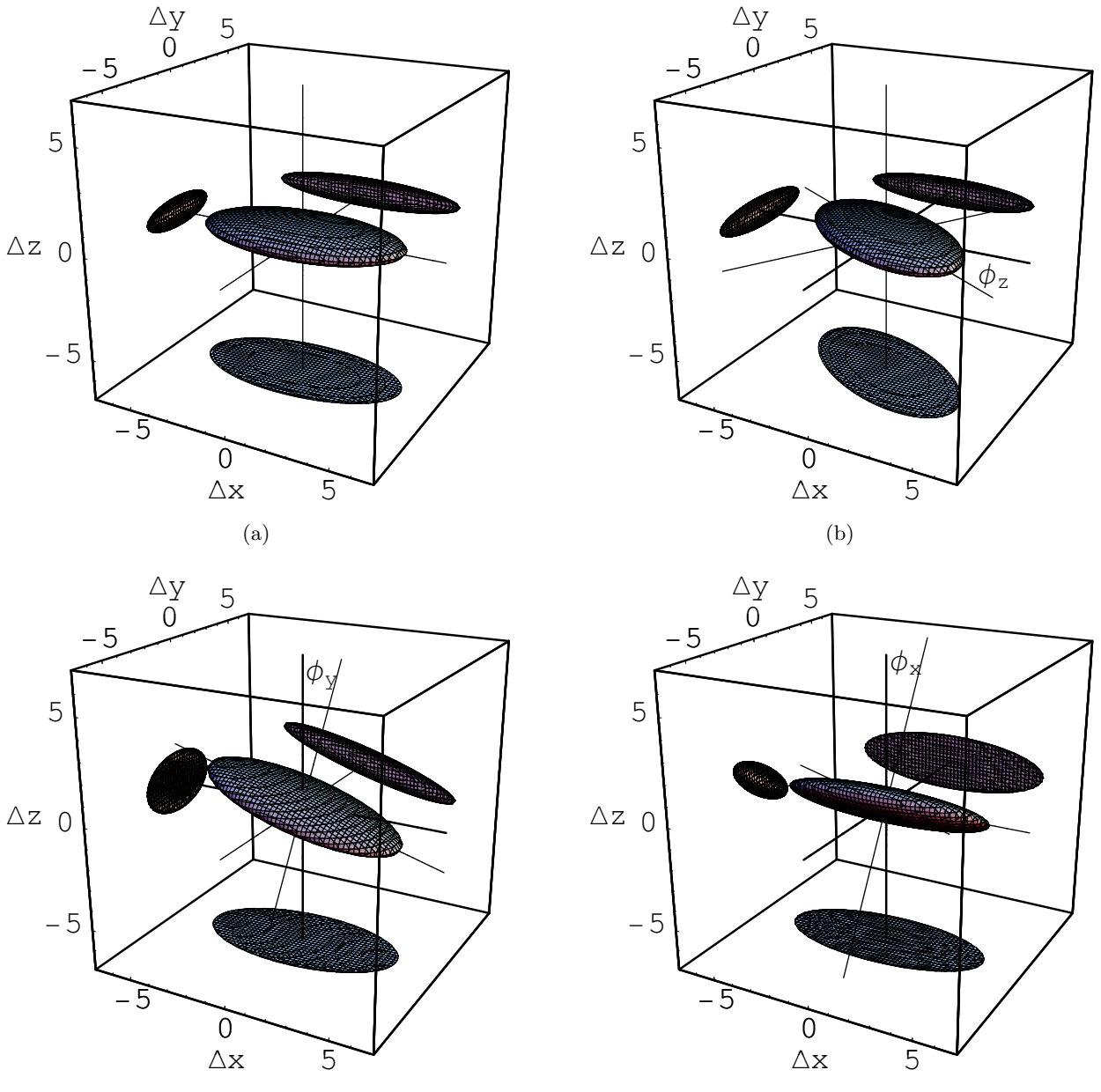

Figure 1: Isosurface $\bar{R}(\Delta x, \Delta y, \Delta z; a, b, c) = \exp\left(-\Delta x^2/a^2 - \Delta y^2/b^2 - \Delta z^2/c^2\right) = 1/e$ for $a = 5$, $b = 2.5$, and $c = 0.75$: (a) $\phi_x = \phi_y = \phi_z = 0$, (b) orientation rotation around z by $\phi_z = 30°$, (c) dip rotation around y by $\phi_y = -15°$, and (d) tilt rotation around x by $\phi_x = 30°$.

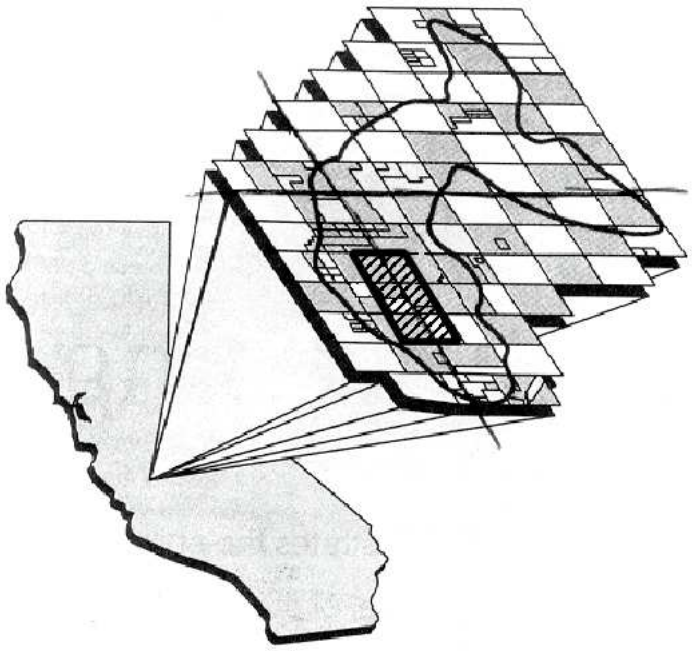

Figure 2: Location map of the Coalinga giant oilfield. The blocks denote one square mile. The hashed area outlines the seismic data volume used in this example.

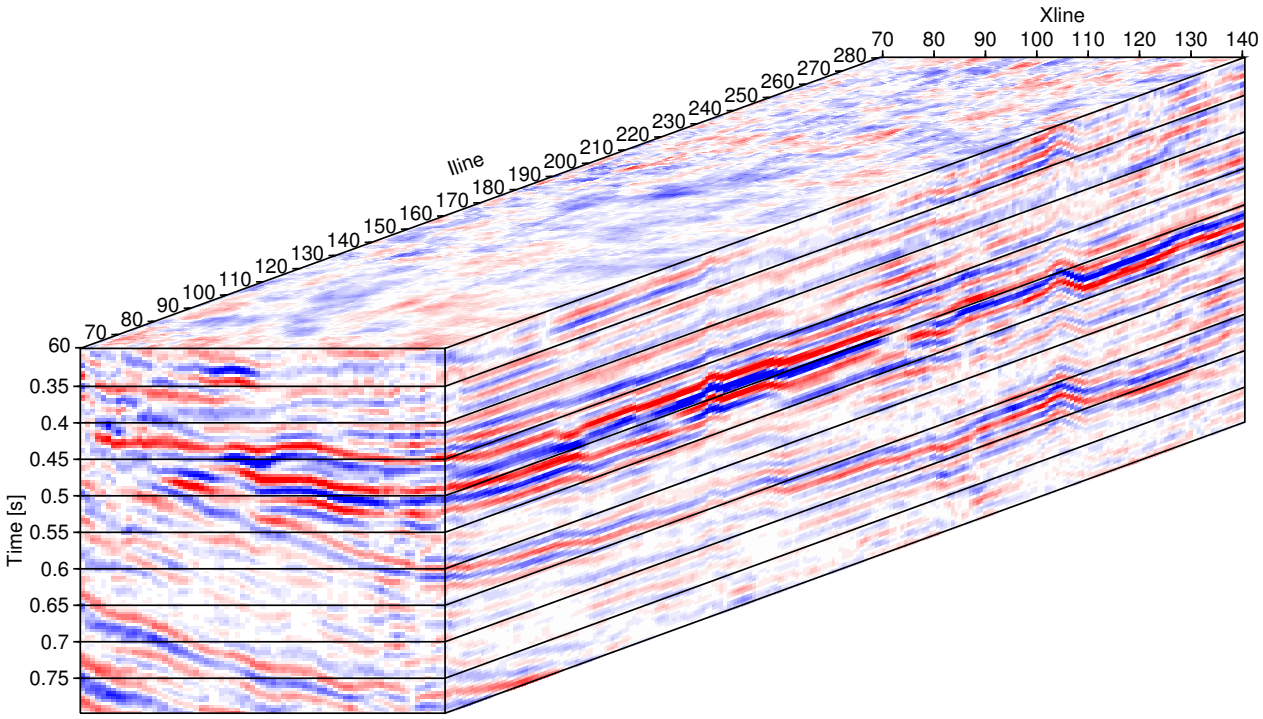

Figure 3: Time-migrated seismic datacube from the Coalinga field. The volume has been flattened at the 400 ms reflector. Red (blue) denotes negative (positive) amplitudes.

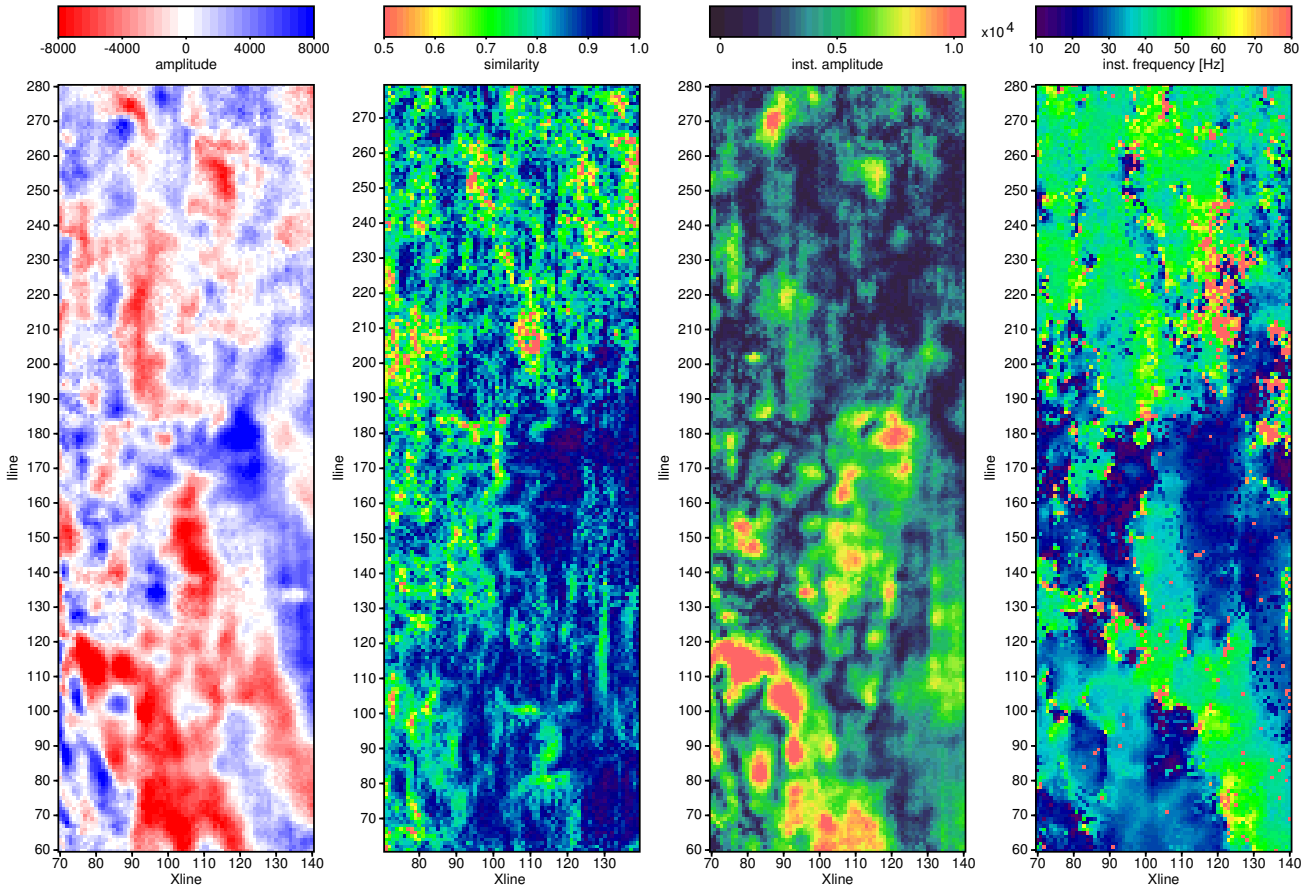

(a) amplitude (b) similarity (c) instantaneous amplitude (d) instantaneous frequency

Figure 4: Seismic attribute slices 40 ms below the Top Temblor.

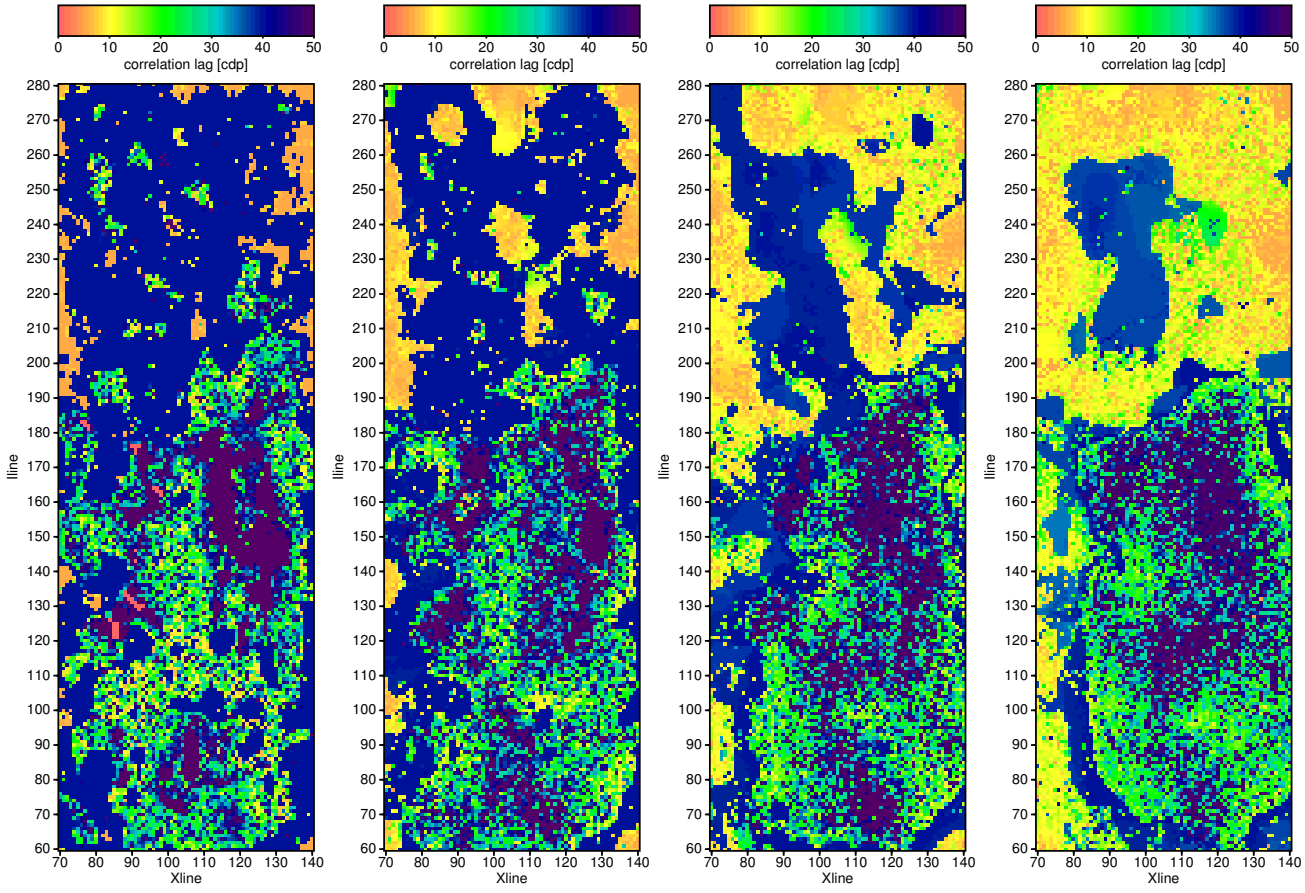

(a) $5\Delta t \times 5\,\text{cdp} \times 5\,\text{cdp}$ (b) $9\Delta t \times 9\,\text{cdp} \times 9\,\text{cdp}$ (c) $13\Delta t \times 13\,\text{cdp} \times 13\,\text{cdp}$ (d) $17\Delta t \times 17\,\text{cdp} \times 17\,\text{cdp}$

Figure 5: Long correlation heterogeneity parameter a at a depth of 40 ms below Top Temblor for different probe volumes.

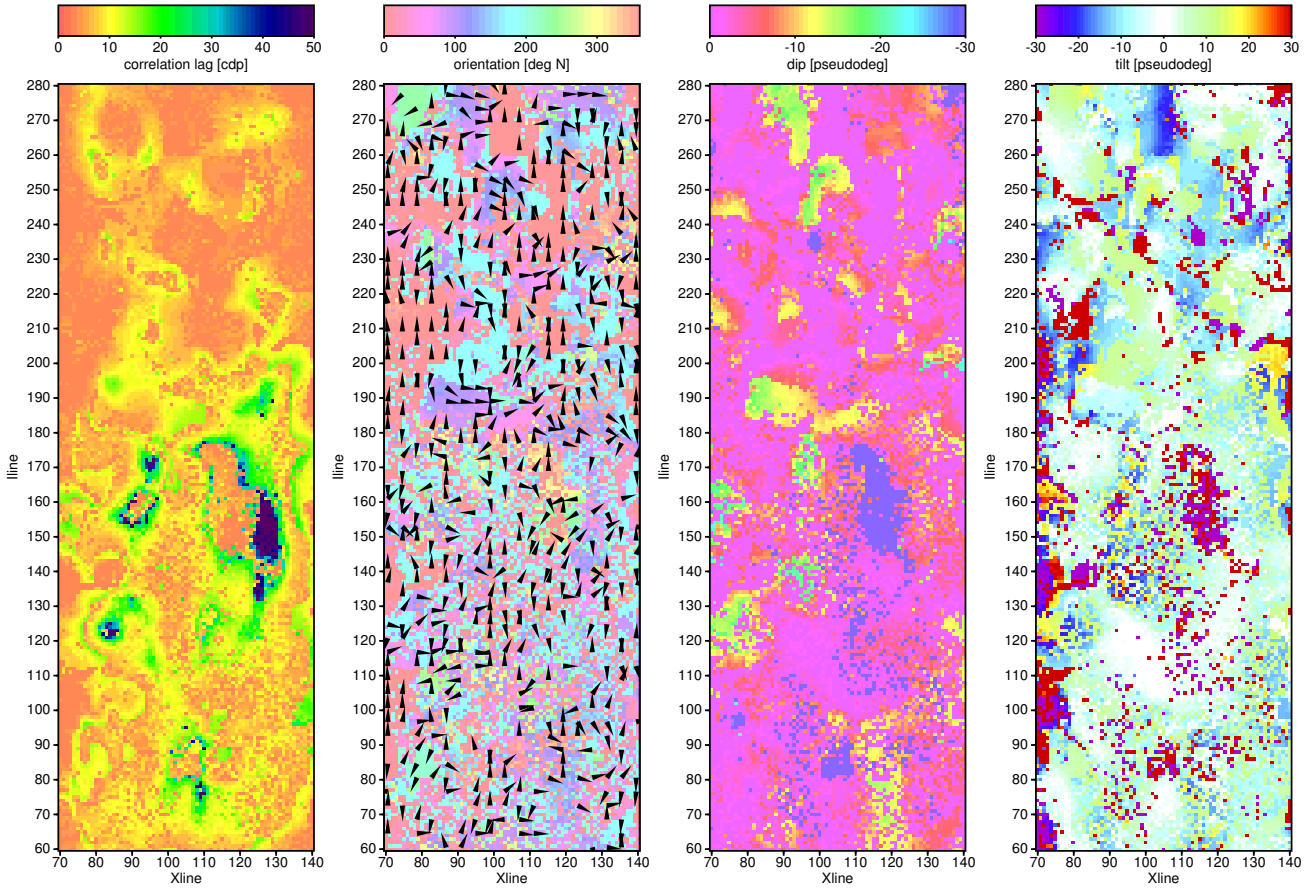

(a) correlation length b (b) orientation ϕ_z (c) dip ϕ_y (d) tilt ϕ_x

Figure 6: Heterogeneity parameters 40 ms below Top Temblor. Orientation ϕ_z is indicated both by color and arrow direction. A missing arrow denotes vanishing dip.

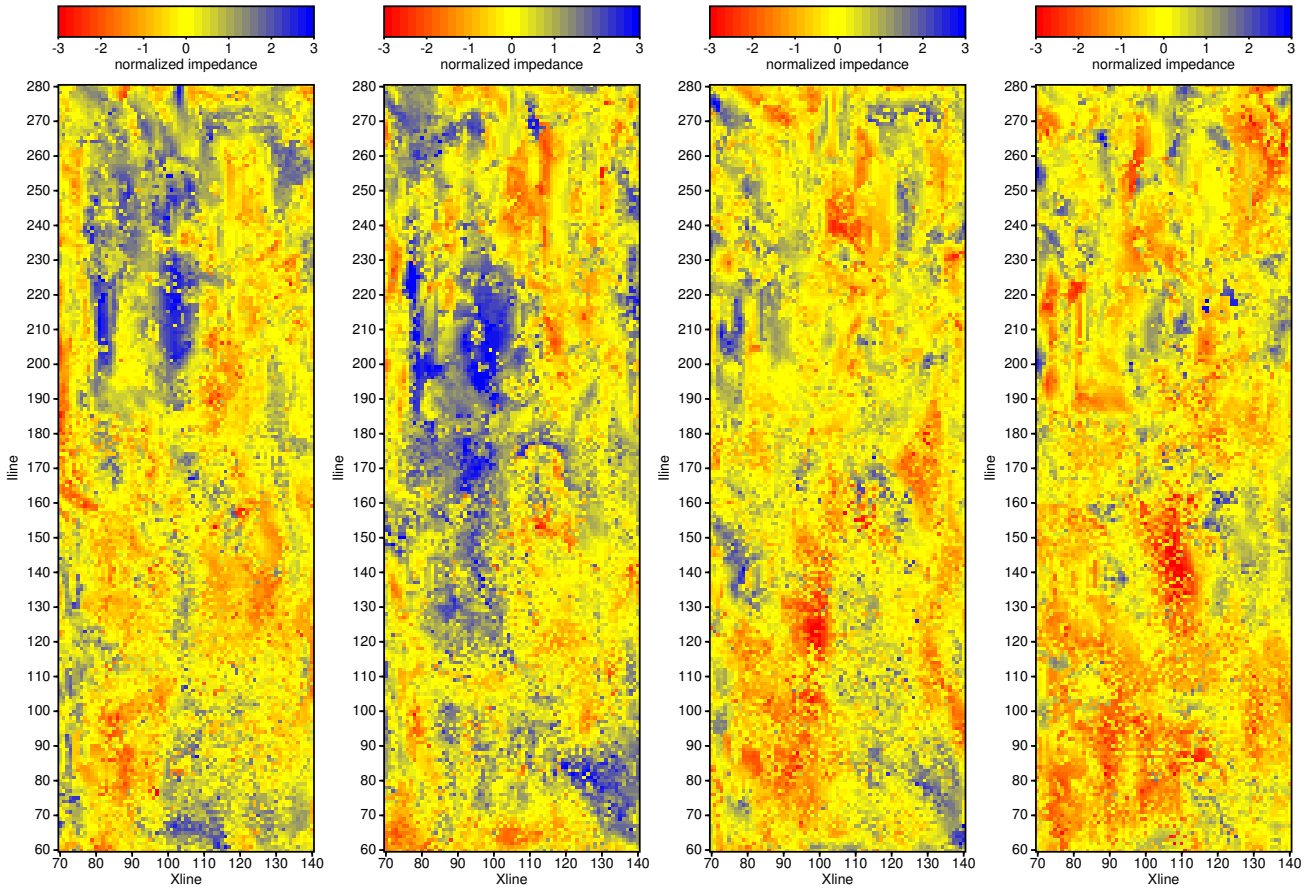

(a) (b) (c) (d)

Figure 7: Different realizations which are compatible with the heterogeneity cubes.

Object-Based Stochastic Facies Inversion: Theory and Application to Hydrocarbon Reservoirs

E. Nowak and M. G. Imhof, Virginia Tech

Introduction

Reservoir models are a necessary tool during the exploitation of hydrocarbon reservoirs. Such realizations may be generated by defining the model and its parameters that dictate the composition and internal structure of a reservoir.

Core and wireline log data provide a detailed account of the lithologic composition of a reservoir and are capable of identifying small-scale heterogeneities at the well locations. Because these data are incapable of resolving features that deviate from the well path, log correlation and deterministic seismic interpretations are often used to interpolate between wells. The seismic reflection interpretations provide a means of resolving lateral and vertical heterogeneity between wells, but are subject to a ¼ wavelength resolution limit. Due to resolution limits of deterministic seismic interpretations and the one dimensional nature of core and wireline log data, conventional techniques of generating reservoir models rely on geologic intuition and modern or outcrop analogs to further characterize a reservoir. For example, to characterize a reservoir exhibiting channelized features, geologic intuition and analogs aid in defining the sinuosity of small-scale channels, width-to-depth ratios of associated facies, and how these associated facies are positioned spatially with respect to one another.

Object-based reservoir models build a realization by emplacing channels, barriers, and other objects using parameters such as sinuosity and aspect ratios. The purpose of the object-based stochastic facies inversion is to reduce the dependence on geologic intuition and analogs when generating realizations of hydrocarbon reservoirs. We are working on an object-based stochastic facies inversion, which determines model parameters and their ranges from all available data, including seismics. The inversion process begins with an initial reservoir realization, which is converted to seismic velocity and density and used to calculate synthetic seismic data. The synthetic seismic data is compared to the observed seismic data. Based on this comparison, a new set of parameters is chosen which are consistent with all other data. The new set of parameters is used in the object-based reservoir simulation to generate a new realization, which is conditioned to the well logs. This iterative process continues until an acceptable match between the realization and data is attained.

We believe that a more quantitative approach to defining these parameters will generate reservoir models with improved correlation between predicted and recorded production histories.

Methodology

Object-Based Stochastic Reservoir Modeling

The process of generating a reservoir realization through an object-based stochastic process is a function of several statistical parameters. These parameters typically include, but are not limited to: mean width, thickness, and length of the included objects, standard deviations associated with these aspect ratios, volumetric proportions of the included objects, mean amplitudes and sinuosity of channels, and rules governing how these objects are positioned spatially with respect to one another. The objects included in the modeling process can be of arbitrary or geologically significant shapes, such as half elipsoids, domes, prisms, and rectangular cubes representing channels, bars or dunes, splays, and barriers (respectively).

The stochastic process initiates by pseudo-randomly emplacing the objects based on their respective statistical parameters (mean and variance values) within a model space. If this realization honors the volumetric proportions of the included objects within some degree of tolerance and predefined interval facies logs, the realization is accepted. However, if the realization does not honor these parameters, which are derived solely on core and wireline log interpretation, subsequent realizations are generated until the geologic criterion is achieved.

The volumetric proportion of objects can be determined from the core and wireline log data, however the remaining statistical parameters (mean and variance of the aspect ratios associated with the objects, mean amplitudes and sinuosity of channel systems, and the location rules) need to be defined. To emphasize the significance of accurately defining these statistical parameters, consider the three reservoir realizations depicted in Fig. 1a, 1b, and 1c in the Appendix. Each of these realizations was generated with different statistical parameters and location rules but conditioned to the same volumetric proportion of objects and interval facies logs (i.e. the geologic criterion). The differences with respect to the placement of the channel and barrier objects is apparent among these three realizations, thus well planning would have to be equally variable to successfully produce hydrocarbons from reservoirs that mimic these realizations.

Inversion

In principle, the statistics of the architectural objects and the location rules can be determined from observed seismic data by nonlinear inversion, however the nonlinearities are strong enough that a linearized least-squares inversion would probably not find the optimum model. In this study we employ a guided search technique for nonlinear inversion, simulated annealing (SA), to determine the optimal solution for the model parameters.

The simulated annealing algorithm is employed to find a model m that minimizes a normalized error-energy function E or maximizes a cross correlation between observed

and synthesized data. For the purposes of this study the model space m_{rs} is populated with the statistical parameters necessary to generate a reservoir realization, equ. (1) modified from (Sen et al.,1992).

$$m_{rs} \equiv \begin{bmatrix} m_{1,1} & m_{2,1} & \cdots & m_{R-1,1} & m_{R,1} \\ m_{1,2} & m_{2,2} & \cdots & m_{R-1,2} & m_{R,2} \\ \vdots & \vdots & \ddots & \vdots & \vdots \\ m_{1,S-1} & m_{2,S-1} & \cdots & m_{R-1,S-1} & m_{R,S-1} \\ m_{1,S} & m_{2,S} & \cdots & m_{R-1,S} & m_{R,S} \end{bmatrix} \tag{1}$$

where each row (1 through S) corresponds to a particular statistical parameter and each column (1 through R) corresponds to a possible value that the respective parameter can attain. For instance $m_{1\rightarrow R,1}$ may correspond to R possible values for mean channel widths, $m_{1\rightarrow R,2}$ may correspond to the R possible standard deviations associated with the mean channel widths, etc.

An initial model $m_{1,1\rightarrow S}$ is selected and used to parameterize the generation of a realization in the same fashion as stated above. Subsequent to forward modeling, which is discussed in a later section, an energy function E is evaluated via a normalized cross-correlation between each synthesized u_s and observed u_o seismic traces, equ. (2) modified from (Sen et al.,1992).

Time Domain

$$E(m_{rs}) = \frac{u_o \otimes u_s}{(u_o \otimes u_o)^{\frac{1}{2}} (u_s \otimes u_s)^{\frac{1}{2}}}$$

Fourier Domain

$$E(m_{rs}) = \frac{2 \times (u_o u_s^*)}{u_o u_o^* + u_s u_s^*} \tag{2}$$

where '⊗' denotes cross-correlation and '*' denotes the complex conjugate. The model attains the mean energy value after all u_s and u_o have been evaluated. This process repeats for all R values of the current parameter maintaining constant values for $m_{1,2\rightarrow S}$. A probability distribution P is evaluated, via equ (3) (Sen et al.,1992), which calculates the likelihood that any one of the R values of the current parameter is correct based on the energy function E.

$$P(m_{rs}) = \frac{e^{-E(m_{rs})/T}}{\sum_{r=1}^{R} e^{-E(m_{rs})/T}} \qquad T = T_0 \times 0.99^i \tag{3}$$

A new value for the current parameter is retained based on this probability distribution and the process continues to the next parameter maintaining constant values for parameters $m_{r,1}$ and $m_{1,3\rightarrow S}$. An iteration i in the annealing process constitutes the completion of evaluating the S^{th} parameter, the temperature T is lowered, and the cycle repeats until an acceptable match between the observed and synthesized data is attained.

To establish a computationally efficient cooling process, experimental trials are often performed before selecting the initial temperature T_0.

Forward Modeling

For the purposes of this study, fourier synthesis of seismic data provides a computationally efficient means of generating synthetic seismic data. A convolution model has been adopted to generate the synthetic post-stack (zero offset) seismic data. Each realization is converted to an impedance volume based solely on the occurrence of the architectural objects and associated impedance values. On a trace by trace basis, the impedance volume is converted to reflectivity R, via equ (4).

$$R_t = \frac{v_t \rho_t - v_{t+1} \rho_{t+1}}{v_t \rho_t + v_{t+1} \rho_{t+1}} \tag{4}$$

The synthetic seismic data results from the convolution of the reflectivity series and a standard 60 Hz Ricker wavelet. When this operation is performed in the fourier domain it simplifies to a mere multiplication. Because the necessary calculations during the inversion process (ie energy function) can be performed in the fourier domain, the synthesized seismic data need not be transformed back to the time domain.

Synthetic Experiments

In order validate the potential success of our object-based stochastic facies inversion the technique was applied to synthetic geologic scenarios. If the results were favorable when applied to synthetic data, which is devoid of interpretation errors and data noise, then the technique has the potential to be successful when applied to field data.

A reservoir model was generated through the object-based simulation process and deemed observed. A two-parameter by five-value model space, consisting of mean channel widths and thicknesses, was generated symmetrically around the true values for these parameters. Each model parameter value was allowed to vary ±20% and ±40% the true value. As shown on Fig. 2a in the Appendix, the inversion process converged on the optimum solution of model parameters (i.e. energy value = -1) value by the 9th iteration. Also shown on the suite of graphs, Fig. 2b, the parameter value selection process became highly focused by the 8th and 9th iteration, causing the inversion process to converge on the correct model parameter values.

A second suite of synthetic experiments involved modeling a channelized reservoir with objects of arbitrary geometries (ie. rectangular prisms). As opposed to the previously described experiment the inversion process did not converge to a perfect cross correlation. However, these experiments did attain an E=-0.307. Even with this diminished cross correlation between the model deemed observed and resulting

realization many similarities can be observed between these two models as shown in Fig. 2c and 2d.

Coalinga Heavy Oil Field

Our method of generating reservoir realizations is applied to Chevron's Coalinga heavy oil field in southwestern California. The Coalinga field is a mature field with an abundance of core and wireline log data. The relative abundance of geologic and petrophysical data makes this a suitable reservoir to assess the results of our realizations since wells can be excluded and be used for control.

Temblor Formation

The Coalinga field has been oil and gas productive from the Temblor formation since the early 1900's. This unconformity-bounded reservoir can be subdivided into three main depositional zones, refer to Fig. 3a in the Appendix. The basal zone is bounded at the base by a major erosional surface, Base Temblor, and at the top by an unconformity designated #2. Unconformity #2 marks the transition to tide and wave dominated shoreline facies, which is in turn capped by an unconformity, designated #1. This unconformity defines the transition to subtidal dominated facies, which is bounded at the top by the Top Temblor.

Currently, production is focused in the basal zone of the Temblor formation and is aided by steam injection. Two marginally conflicting interpretations of the depositional environment associated with this basal zone have been observed in literature. Bate, 1984, characterized this basal zone as channel-cut sands containing impermeable barriers. It was suggested that these impermeable barriers are a result of shale drapes bounding the channels of an ancient braided river system. These impermeable barriers compartmentalize the reservoir hence hindering production. Bridges et al., 2002, describes two dominate facies types within this basal zone, incised valley facies overlain by estuarine facies. Incised valley facies types were characterized by stacked channel deposits associated with incisions exhibiting high topographic relief. A general fining upward succession of sediment from the fluvial channel deposits to estuarine channel deposition conforms to a relative sea level rise during the Miocene.

Well Data

Based on the interpretation of core data, the Temblor formation is composed primarily of seven lithotypes. These lithotypes include: sands, burrowed sands, laminated sand, silt and clay, fossiliferous sand and clay, burrowed clay, limestone, and calcareous cemented sediment. From these core interpretations the volumetric proportions of the seven

lithotypes were determined and interval facies logs were generated and used as the geologic control during the simulation process. Where the core data was accompanied by sonic and density logs, the distribution of acoustic impedance as a function of lithotype was determined as shown on Fig. 4a through 4g. These distributions are necessary to convert the realization to an impedance volume during the forward modeling stage of the inversion process.

Seismic Attribute Analysis

Regardless of the geologic interpretation of this basal zone of the Temblor formation, there is evidence of sinuous features. These sinuous features, either channel sands resulting from a braided river environment (Bate, 1984) or amalgamated fluvial channels overlain by estuarine channel deposits (Bridges, et al., 2002), can be observed in the form of seismic attributes.

Seismic attributes provide a means of interpreting data from different points of view, which often results in new insight not otherwise evident. These attributes are the result of transformations or calculations performed solely on the time series seismic data. Fig. 3b represents a seismic time slice extracted 108 ms below the Top Temblor horizon, refer to Fig. 3a. Fig. 3c and 3d display the results of two seismic attributes, coherency and instantaneous amplitude (respectively), which were calculated directly from the seismic data and correspond to the same time slice depicted in Fig 3a.

Coherency, as an attribute, has recently received much attention for identifying lateral changes in acoustic impedance caused by faulting and meandering channels (Marfurt, et al., 1998). It is a measure of similarity or dissimilarity, via a cross-correlation similar to equ. (2), between isolated intervals of adjacent seismic traces. As observed on Fig. 3c in the Appendix, the dark blue zones, corresponding to high coherence values, represent areas of seismically similar material. The green and red zones correspond to reduced coherency values, representing transition zones of seismically dissimilar material.

Instantaneous amplitude is a continuous measure of reflectivity strength, which is also governed by impedance contrasts, along a single seismic trace. The vector length of amplitude values and their corresponding quadrature amplitude values along the recorded seismic trace result in the instantaneous amplitude assessment, based on (Yilmaz, 1987) and (Taner, et al., 1979). Fig. 3d in the Appendix displays an instantaneous amplitude time slice corresponding to the seismic time slice depicted in Fig 3b.

The extent of the steam injection (shown in red on Fig. 3d) is observed by elevated amplitude values on the instantaneous amplitude time slice. These same areas are

coincident with very coherent areas (shown in dark blue on Fig. 3c) on the coherency time slice. The presence of stream (ie. high amplitude anomalies) in a seismically coherent zone suggests that this area is somewhat homogeneous and permeable; however the steam front does appear to be abruptly truncated against some rather sinuous features. These sinuous features can be observed on both the coherency (in green) and instantaneous amplitude (in dark blue) time slices, Fig. 3c and 3d (respectively).

The two realizations, shown on Fig. 3e and 3f, correspond to the same time slice as the aforementioned attribute figures. These realizations were forced to honor the same lithology logs and volumetric proportions of facies using arbitrary geometric shapes. As can be seen on Fig. 3f there is a rough correlation between the sand and burrowed sand lithotypes and the moderately incoherent areas on Fig. 3c.

These features are expected to contribute to the heterogeneity indigenous to the basal zone of the Temblor formation and a cause for production inefficiencies. Based on the relative abundance of geologic and the petrophysical control and predominant sinuous features associated with the basal zone of the Temblor formation, the Coalinga heavy oil field is deemed a suitable candidate to assess our technique of generating reservoir realizations.

Discussion

Based on the results of the preliminary synthetic experiments, the object-based stochastic facies inversion has the potential to be successful when applied to hydrocarbon reservoirs. By incorporating the seismic waveform inversion as a proxy to geologic intuition and analogs, the optimum solution for the model parameters was attained via the simulated annealing guided search technique for nonlinear inversion. However, there is one main underlying assumption bestowed in this experiment. The reservoir model, deemed observed, was generated by the object-based simulation process. This implies that natural reservoirs can be modeled by an optimum set or sets of statistical parameters. Addressing this assumption is the focus of the proposed work: the object-based stochastic facies inversion will be applied to the Coalinga heavy oil field.

In the event that the results are not favorable when this technique is applied to the Temblor formation, meaning there is a low correlation between the recorded and synthesized seismic data, an alternative does exist. The adaptation manifests itself in the forward modeling algorithm. In the previous sections post-stack seismic wavefields provided the means of assessing the correlation between the observed reservoir and the synthesized realization. By altering the forward modeling algorithm to accommodate source-receiver offsets, pre-stack seismic wavefields can be used for the assessment. Pre-stack seismic data has the advantage of increased ray coverage, minimal processing

artifacts, and no waveform averaging effects due to stacking. However, these advantages exist at the cost of increased computation time and decreased signal-to-noise ratio.

Efforts will also be made to test the robustness of our methodology, through the use of additional synthetic experiments, in a variety of geologic scenarios. For example, it is possible that a sand interval observed in a well can be interpreted as a channel or sheet sand facies type. For example, during the inversion process the sand interval is assumed to correspond to a channel facies type, and the mean channel width is included as a model parameter. The inversion process may yield a channel whose width extends past the limits of the model space, hence a sheet sand, or a narrower feature, may be interpreted as a channel facies type.

To reiterate the importance of quantitatively defining the statistical parameters that dictate the internal distribution of facies within a reservoir refer to Fig. 3e and 3f. The variability between these two realizations is apparent, however the rough correlation between the sand and burrowed sand lithotypes with the moderately incoherent areas on Fig. 3c would not have been possible if the average length and width of the objects were not increased from those used in Fig. 3e. Hence, it is the aim of the object-based stochastic facies inversion to refine these statistical parameters to maximize the correlation between the realization and the recorded seismic and well data.

Conclusion

If successful, the results of our adaptation to conventional techniques of generating reservoir models will reduce the cost of extracting hydrocarbons during the production stage of a reservoir. This cost reduction would be observed through improved injection and extraction well planning resulting from reservoir models that more closing mimic the producing reservoir.

References

Bate, Matthew, Adam, 1984, Temblor and Big Blue formations: interpretation of depositional environment sequence on Coalinga anticline, Fresno County, California: Masters Thesis, Stanford University.

Bridges, Robert, A., and Castle, James, W., 2002, Local and regional tectonic control on sedimentology and stratigraphy in a strike-slip basin: Miocene Temblor formation of the Coalinga area, California, U.S.A.: Masters Thesis, Clemson University.

Marfurt, Kurt, J., Kirlin, R., Lynn, Farmer, Steven, L., and Bahorich, Michael, S., 1998, 3-D seismic attributes using a semblance-based coherency algorithm: Geophysics, 63, 1150-1165.

Sen, M., K., and Stoffa, P., L., 1991, Nonlinear one-dimensional waveform inversion using simulated annealing: Geophysics, **56**, 1624-1638.

Taner, M., T., Koehler, F., and Sheriff, R., E., 1979, Complex seismic trace analysis: Geophysics, **44**, 1041-1063

Yilmaz, Ozdogan, 1987, Seismic data processing, Society of Exploration Geophysicists, Tulsa, OK.

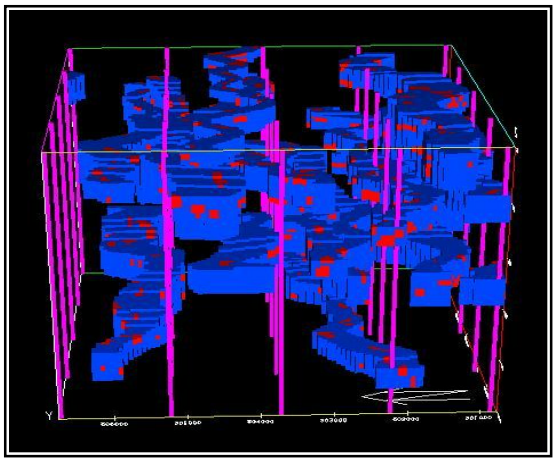

Fig. 1a: A realization generated with the following parameters:

Mean channel thickness:	10
Channel thickness variance:	2
Mean Channel width:	500
Width-thickness correlation:	0.25
Mean channel amplitude:	2000
Channel amplitude variance:	400
Channel sinuosity:	1.25

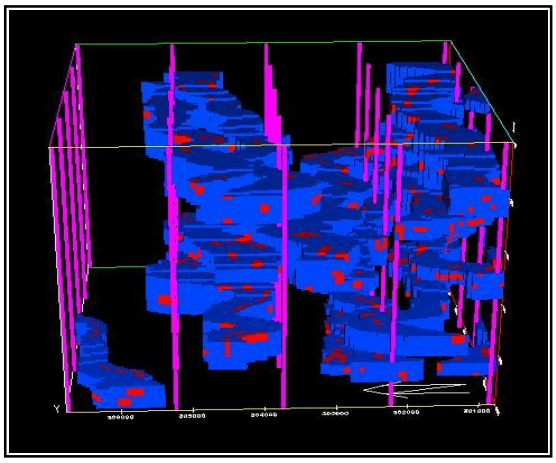

Fig. 1b: A realization generated with the following parameters:

Mean channel thickness:	6
Channel thickness variance:	2
Mean Channel width:	600
Width-thickness correlation:	0.25
Mean channel amplitude:	2000
Channel amplitude variance:	400
Channel sinuosity:	1.25

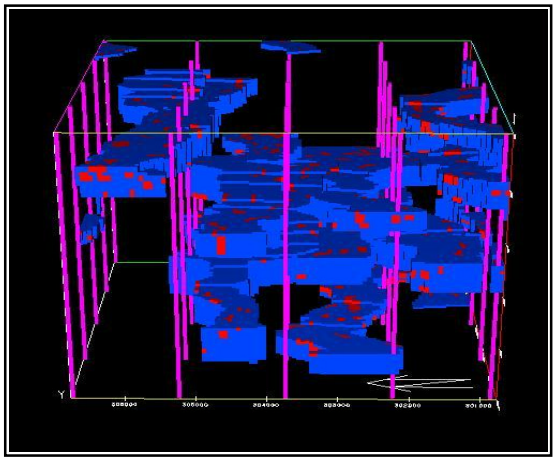

Fig. 1c: A realization generated with the following parameters:

Mean channel thickness:	6
Channel thickness variance:	2
Mean Channel width:	800
Width-thickness correlation:	0.75
Mean channel amplitude:	2000
Channel amplitude variance:	400
Channel sinuosity:	1.25

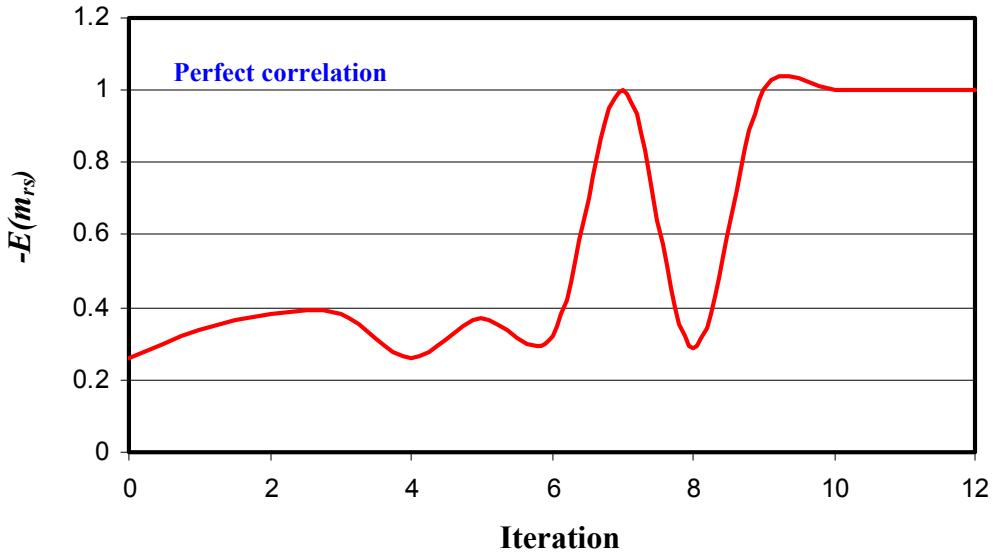

Fig. 2a: Energy as a function of iteration

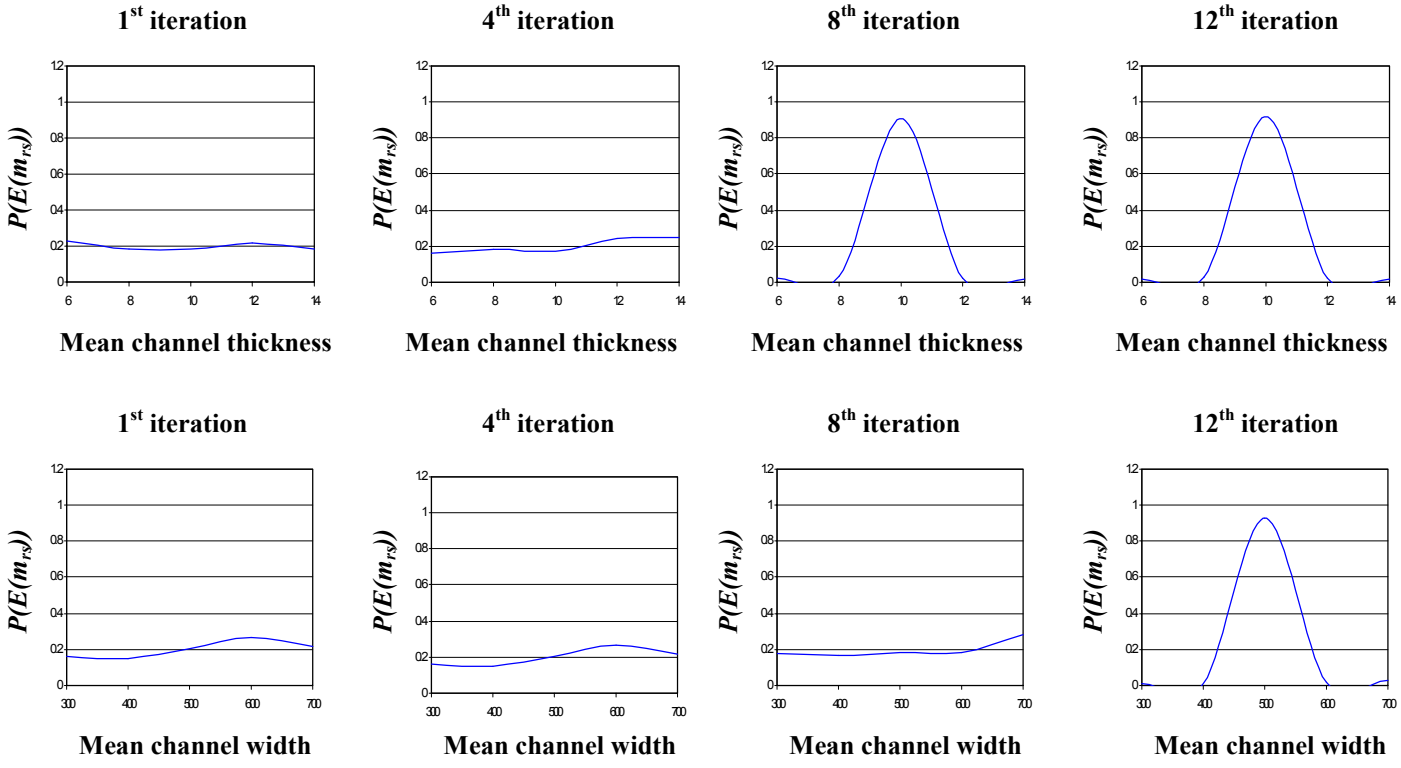

Fig. 2b: Probability distribution of model parameter values with respect to iteration

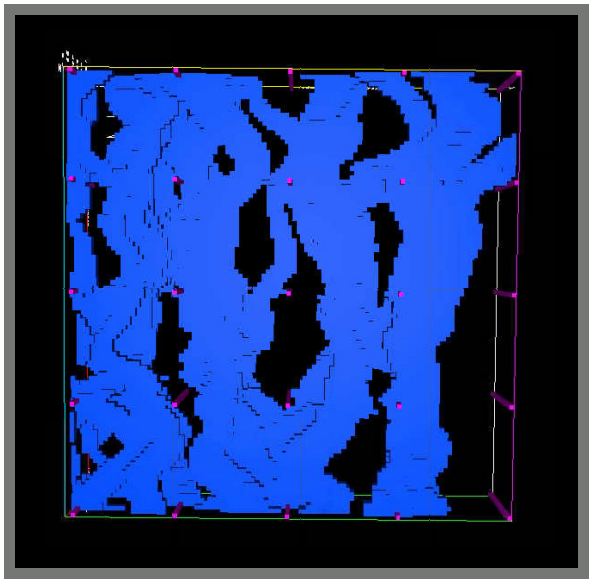

Fig. 2c: Reservoir model deemed observed

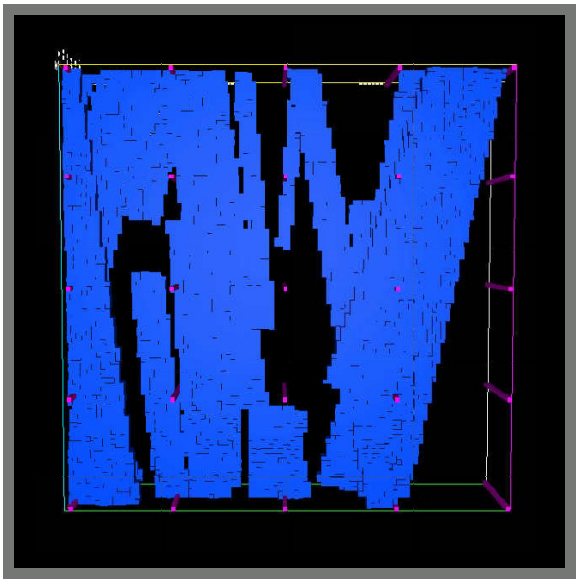

Fig. 2d: Realization of Fig. 2c

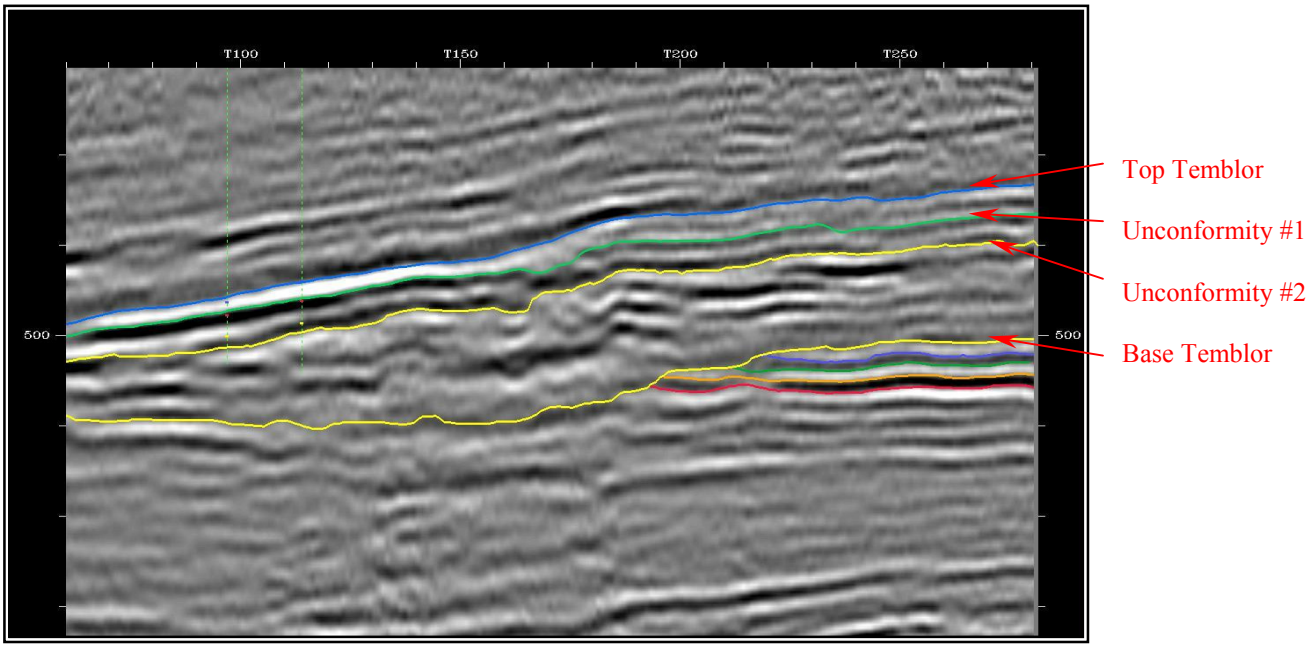

Fig. 3a: Seismic cross-section displaying the three main zones of the Temblor formation.

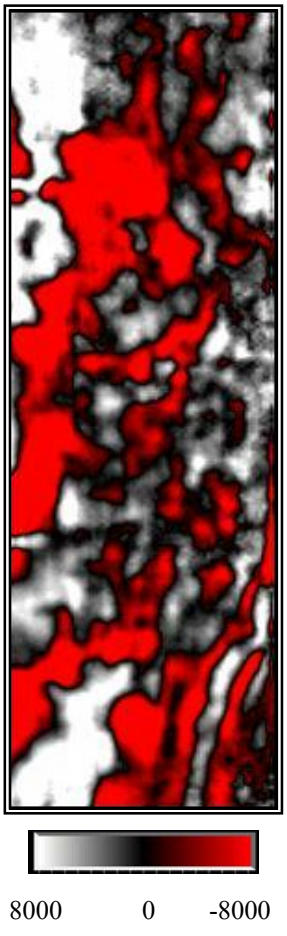

Fig 3b: Seismic

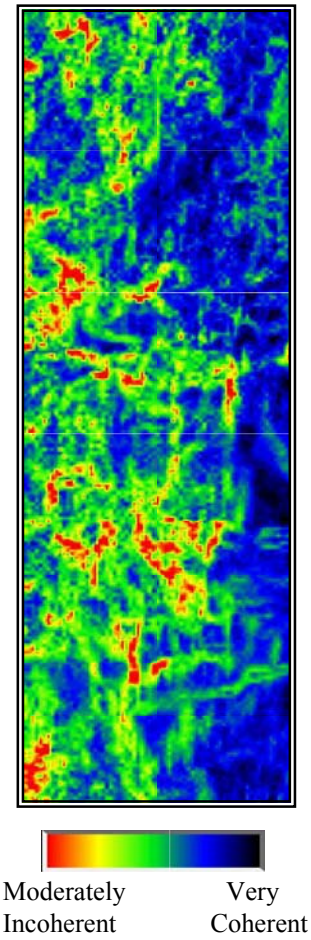

Fig 3c: Coherency

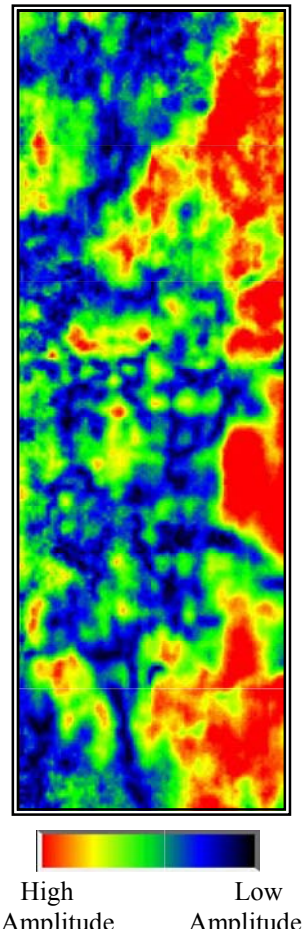

Fig 3d: Instantaneous Amplitude

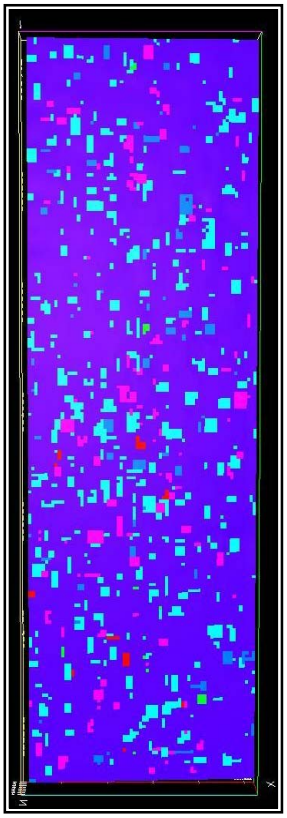

Fig. 3e: Realization
10.0 x 10.0 x 1.0 aspect ratio

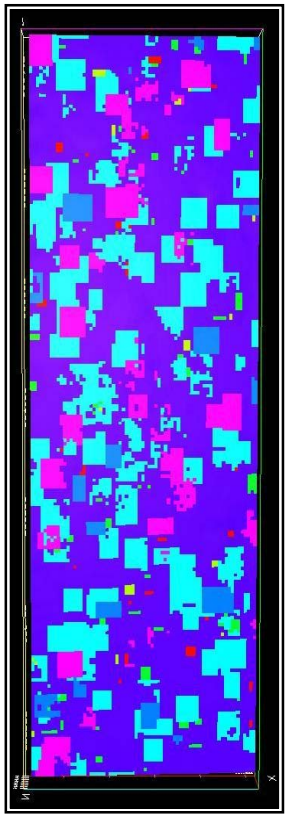

Fig. 3f: Realization
50.0 x 50.0 x 1.0 aspect ratio

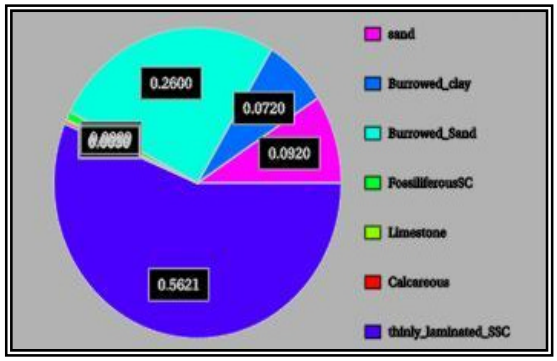

Fig. 4a: Impedance Distribution: Sand

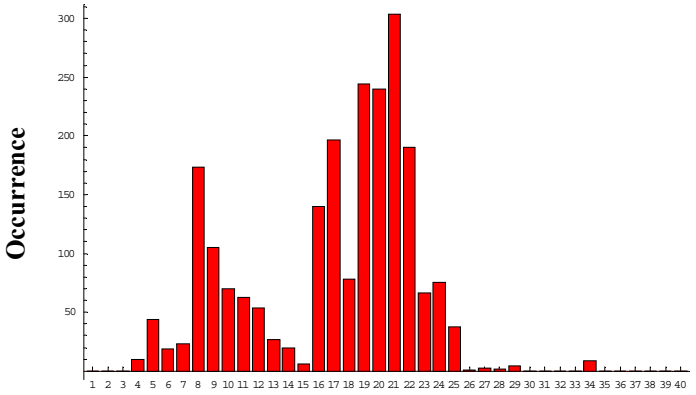

Fig. 4b:Impedance Distribution: Laminated SSC

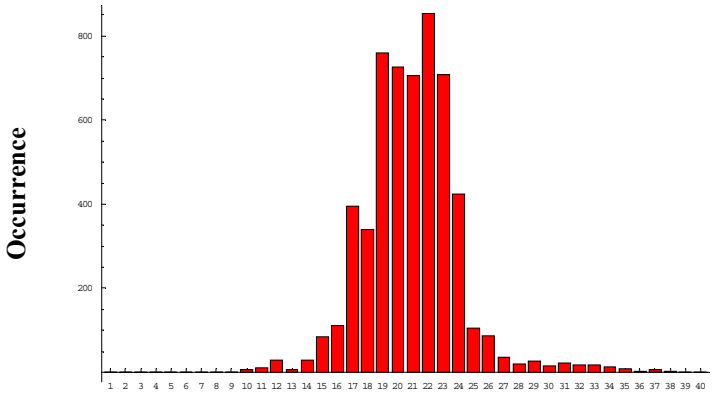

Fig. 4c: Impedance Distribution: Burrowed Clay

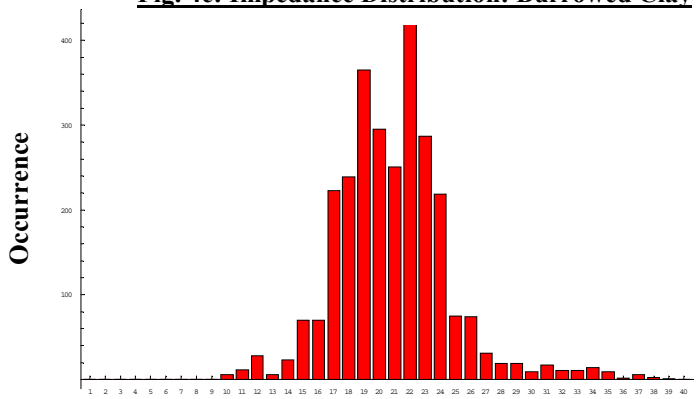

Fig. 4d: Impedance Distribution: Burrowed Sand

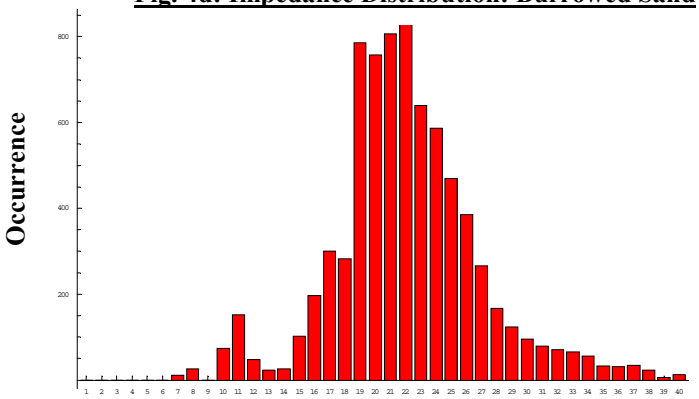

Fig. 4e: Impedance Distribution: Fossiliferous SC

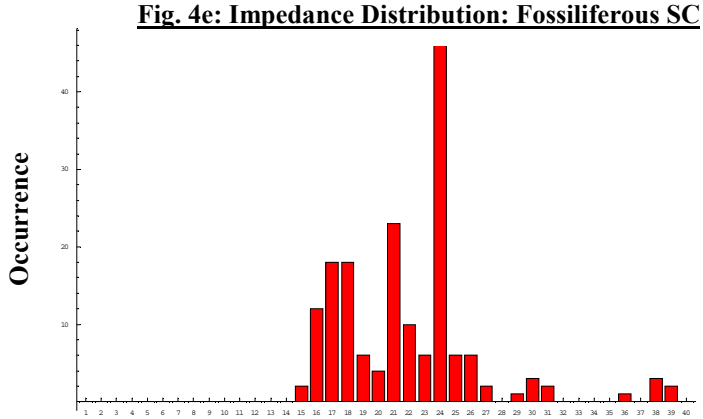

Fig. 4f: Impedance Distribution: Limestone

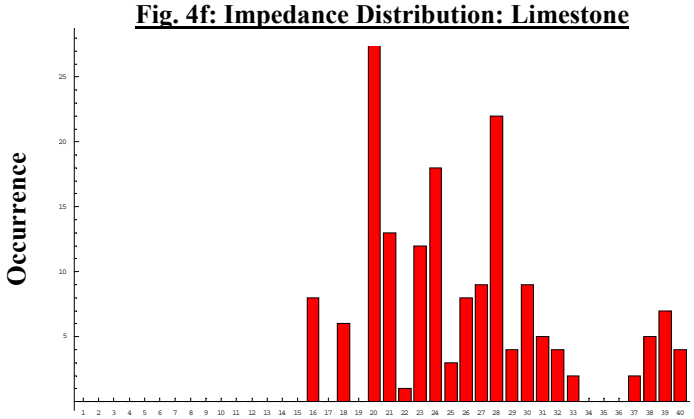

Fig. 4g: Impedance Distribution: Calcareous

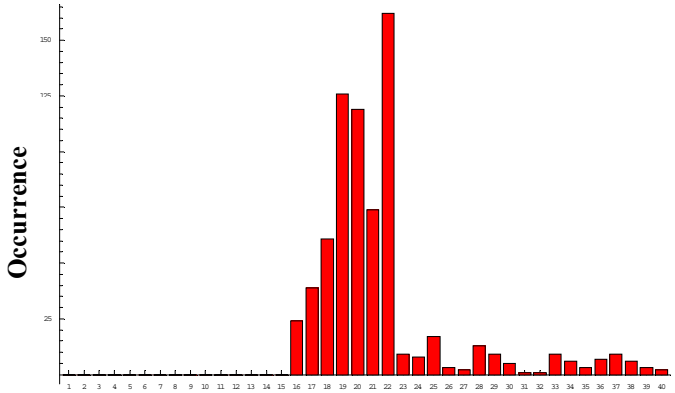

Fig. 4a-4g: Represent the impedance distribution as a function of the lithotypes observed in the core. Please note that:

SC: sand and clay
SSC: sand, silt, and clay
Minimum Impedance: 5000
Maximum Impedance: 25000
Binning Interval: 500

Geologic Heterogeneity Models

J. Castle, Clemson University

SCOPE OF GEOLOGICAL WORK

During the second year of the project, reservoir characterization of the Temblor Formation at West Coalinga Field was performed by investigators at Clemson University. Core descriptions and wireline logs, in addition to core descriptions and outcrop data from a previous related project funded by USDOE (Bridges, 2001; Castle et al., 2002), were used throughout the course of reservoir characterization. This information was applied to developing four types of three-dimensional geologic computer models: deterministic, stochastic lithofacies, stochastic petrophysical, and conditioned. The models were compared to each other and to core descriptions and log data. The results were assessed to determine which of the modeling methods is best suited for integration with seismic data. Additional information on this phase of the project can be found in Mize (2002).

Two field areas from the southern portion of West Coalinga Field were studied (Figure 1). One area is in the north-central portion of section 36D, and contains 28 wells. The other area is located in the northeast portion of section 25D, and contains 66 wells. The two areas were chosen based on their well and four-dimensional (4-D) seismic coverage. Four dimensional seismic is three-dimensional (3-D) seismic data acquired at different times over the same area to assess changes in a producing hydrocarbon reservoir with time. The use of 4-D vs. 3-D seismic allows for the observation of changes in fluid location, fluid saturation, pressure, and temperature.

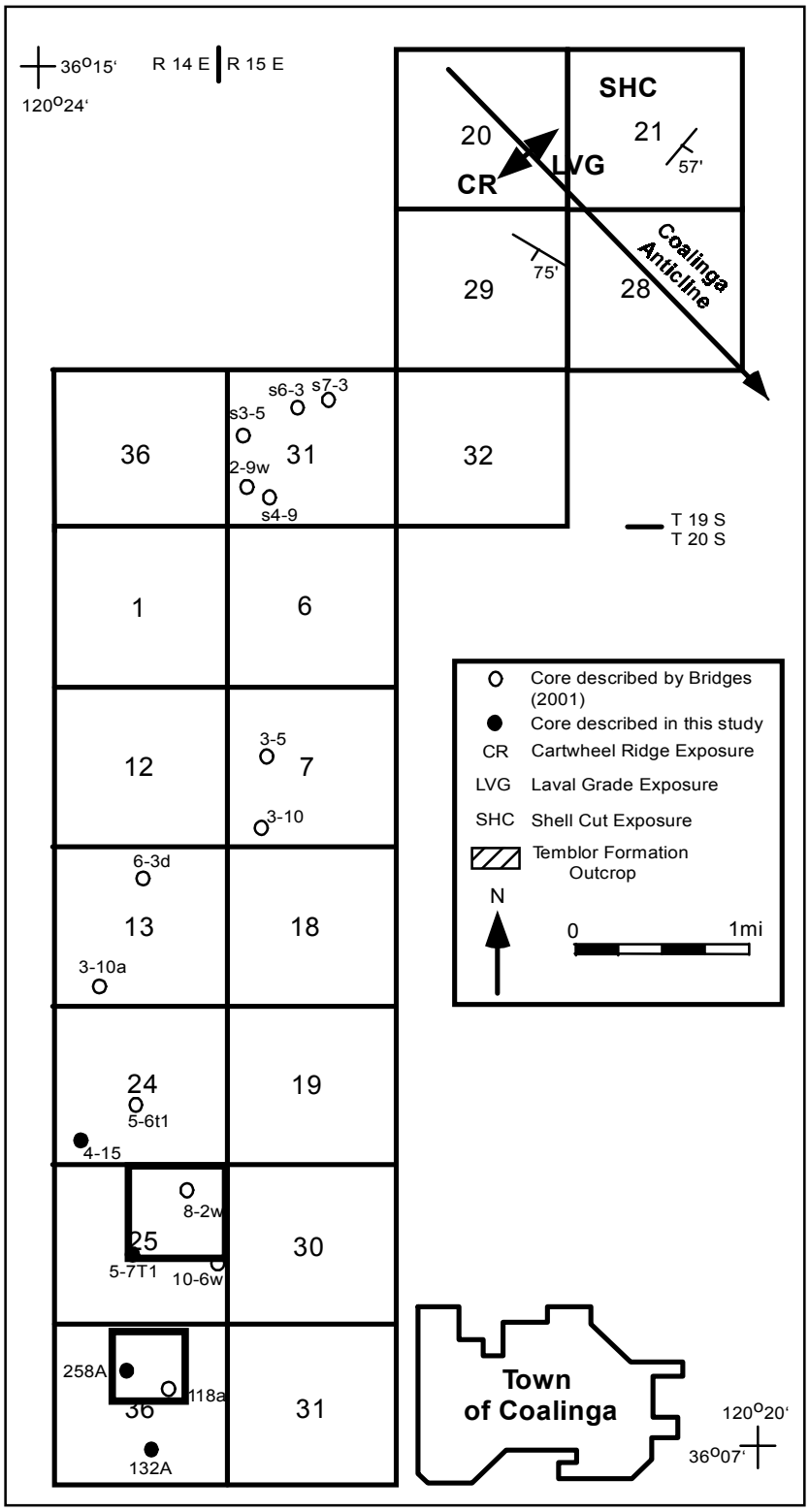

Figure 1. Location of model areas in Sections 25D and 36D.

CORES AND GEOPHYSICAL LOGS

Lithofacies and Lithofacies Groups

ChevronTexaco Production Company in Bakersfield, CA, supplied wireline log data for 94 wells within the study areas and granted access to four cores used in this study. Cores were described at the Chevron Core Warehouse in Richmond, CA, during August 2001. Core descriptions can be found in Mize (2002).

Fourteen lithofacies were identified in core, which were subsequently arranged into 7 lithofacies groups by similarities in grain size, degree of bioturbation, degree of cementation, sedimentary structures, and sorting (Table 1). Lithofacies groups were identified on wireline logs, based on the criteria developed from the logs of from the four cored wells. The sand lithofacies group (1) is characterized by values of 0 to 30% on the scaled gamma ray log (see section on Modeling Methods). The scaled gamma ray signature for this lithofacies group is relatively consistent with small variability. The log signature of the thinly laminated sand, silt, and clay lithofacies group (2) is highly variable with values between 20% and 75%. The scaled gamma ray spikes within the thinly laminated sections are thin in comparison to other spikes. The burrowed clay lithofacies group (3) ranges from 30% to 50% scaled gamma ray and contains one to three consistent spikes with a smooth, not irregular, signature. The burrowed sand lithofacies group (4) has a highly variable (irregular) log signature with several small spikes, and typically ranges from 10 to 40% scaled gamma ray, with scaled gamma ray values near the top of the Temblor ranging from 70% to 100%. Fossiliferous sand and clays (5) are characterized by their location just above

Table 1. Lithofacies Groups.

Lithofacies Group (and Number)	Lithofacies	Deposition
Sand (1)	Clean Sand Crossbedded Sand Pebbly Sand	Barrier/Bar, tidal flat, tidal bars or scour surfaces
Thinly laminated sand, silt, and clay (2)	Clay Silt Interlaminated Sand and Clay Sandy Clay	Wave-dominated, offshore
Burrowed Clay (3)	Burrowed Clay	Tidal flat
Burrowed Sand (4)	Burrowed Sand	Barrier/bar, tidal flat, tidal bars or subtidal
Fossiliferous Sand and Clay (5)	Fossiliferous Sand Fossiliferous Clay	Lagoon or low energy interval
Limestone (6)	Fossiliferous Limestone	Low energy interval, or marine flooding
Calcareous Cemented Sand (7)	Calcareous Cemented Sand Calcareous Pebbly Sand	Scour surface, lag, or diagenetic processes

the base of the Temblor Formation and consist of a large spike (70 to 100%) capped by a smaller spike in scaled gamma ray value. The limestone lithofacies group (6)

occurs generally at the base of the Temblor and has a thickness of 3 to 6 feet. A spike in the density log and a low value in scaled gamma ray are characteristic of the limestone. The carbonate-cemented sands (7) are generally found at the top estuarine and top tide- to wave-dominated shoreline surfaces based on core. Scaled gamma ray values range up to 50%, with a scaled gamma ray spike and common resistivity and density kicks.

Depositional Environments

Based on the core descriptions, three depositional environments are interpreted for the Temblor Formation in the southern part of West Coalinga Field: estuarine; tide- to wave-dominated shoreline; and subtidal (Table 2; see Mize, 2002, for additional discussion of the depositional environment interpretations). The incised valley deposits interpreted by Bridges (2001) and Bridges and Castle (2002) as occurring below the estuarine interval north of the present study area were not observed in core from the southern portion of the field. They also described a separate facies tract between the tide- to wave- dominated shoreline and subtidal facies tracts. This diatomite facies tract consists of diatomaceous clay which grades laterally into burrowed clay towards the southern end of the field. In the northern part of the section 25D study area, thin (3 to 10 feet thick) burrowed clays beds occur immediately below the subtidal lithofacies group. These burrowed clay beds were not separated into a separate depositional environment due to the lack of spatial coverage of the burrowed clays within logs and cores.

Table 2: Physical and biological features of depositional environment intervals in the cores studied.

Well Number	132A	258A	5-7T1	4-15
Chevron Number	IR85310	IO06270	IN50250	IO95320
Section	36D	36D	25D	24D
Subtidal	Abundant horizontal to vertical burrow structures, rare thin clay and limestone beds, mottled appearance	Abundant horizontal to vertical burrow structures, rare thin clay beds and calcareous intervals, mottled appearance	Abundant horizontal to vertical burrow structures, rare thin clay beds, mottled appearance	Abundant horizontal to vertical burrow structures, rare thin clay beds, mottled appearance
Tide- to Wave-Dominated Shoreline	Minor fining upward sequences (4-8 ft.), minor coarsening upward sequence (3-6 ft.), abundant low angle planar cross-bedding, rare ripple cross-lamination, minor clay drapes, rare lag beds with common mud rip-ups and pebbles, faint parallel bedding, abundant burrow structures	Common fining upward sequences (3-6 ft.), minor coarsening upward sequences (3-20 ft.), rare low angle planar cross bedding, rare lag beds with mud rip-ups, common burrow structures	Minor coarsening upward sequences (3-6 ft.), rare low angle planar cross-bedding, rare ripple cross-lamination, minor clay drapes, rare lag beds with common mud rip-ups and pebbles, rare faint parallel bedding, abundant burrow structures	Minor fining upward sequences (2-6 ft.), rare coarsening upward sequences (2-5 ft.), rare to common low angle planar cross-bedding, rare ripple cross-lamination, minor clay drapes, rare lag beds with common mud rip-ups and pebbles, rare faint parallel bedding, common burrow structures
Estuarine	Rare fining upward sequences, common scour surfaces with mud rip-ups and pebbles, rare ripple cross-laminations, common to abundant tabular cross bedding, rare to common clay drapes, rare flaser bedding, abundant shell fragments (clay and sand near base Temblor), rare coarsening upward sequences, rare burrow structures	Rare fining upward sequences, rare scour surfaces with mud rip-ups and pebbles, abundant shell fragments (clay and sand near base Temblor), rare large coarsening upward sequences, rare to common burrow structures	Rare fining upward sequences, common scour surfaces with mud rip-ups and pebbles, rare ripple cross-laminations, common tabular cross bedding, rare clay drapes, Abundant shell fragments (clay and sand near base Temblor), Rare coarsening upward sequences, common burrow structures	Common fining upward sequences, common scour surfaces with mud rip-ups, rare tabular cross bedding, rare clay drapes, abundant shell fragments (clay and sand near base Temblor), abundant burrow structures

Well-to-Well Correlations

Core descriptions were compared with gamma ray and density logs to identify the following bounding surfaces for modeling purposes: base Temblor, clay concentration, top estuarine, top tide- to wave-dominated shoreline, and top Temblor (Figure 2). The base Temblor surface occurs below a thick (70 to 100 ft) coarsening upward sequence and coincides with a spike in the density log, which is also just below a decrease in gamma ray values. This density spike is correlative with the limestone found at the base of the Temblor Formation. The clay concentration surface is placed at the inflection point above a clay concentration at the top of a large fining upward sequence on the scaled gamma ray log. The top estuarine surface corresponds to the inflection point on the top of a large gamma kick at the top of a fining upward sequence, which dominates the upper part of the estuarine interval. The top of the tide- to wave-dominated shoreline surface is at the lower inflection point of a large gamma spike at the base of a coarsening upward sequence of the subtidal interval. This spike generally is the highest gamma ray value within the Temblor Formation, with few exceptions. The subtidal zone has two sets of large gamma spikes (Figure 2; elevation of -710 to -730 feet and -683 to -705 feet). The top Temblor surface is placed above these two sets at the top inflection point of a coarsening upward sequence.

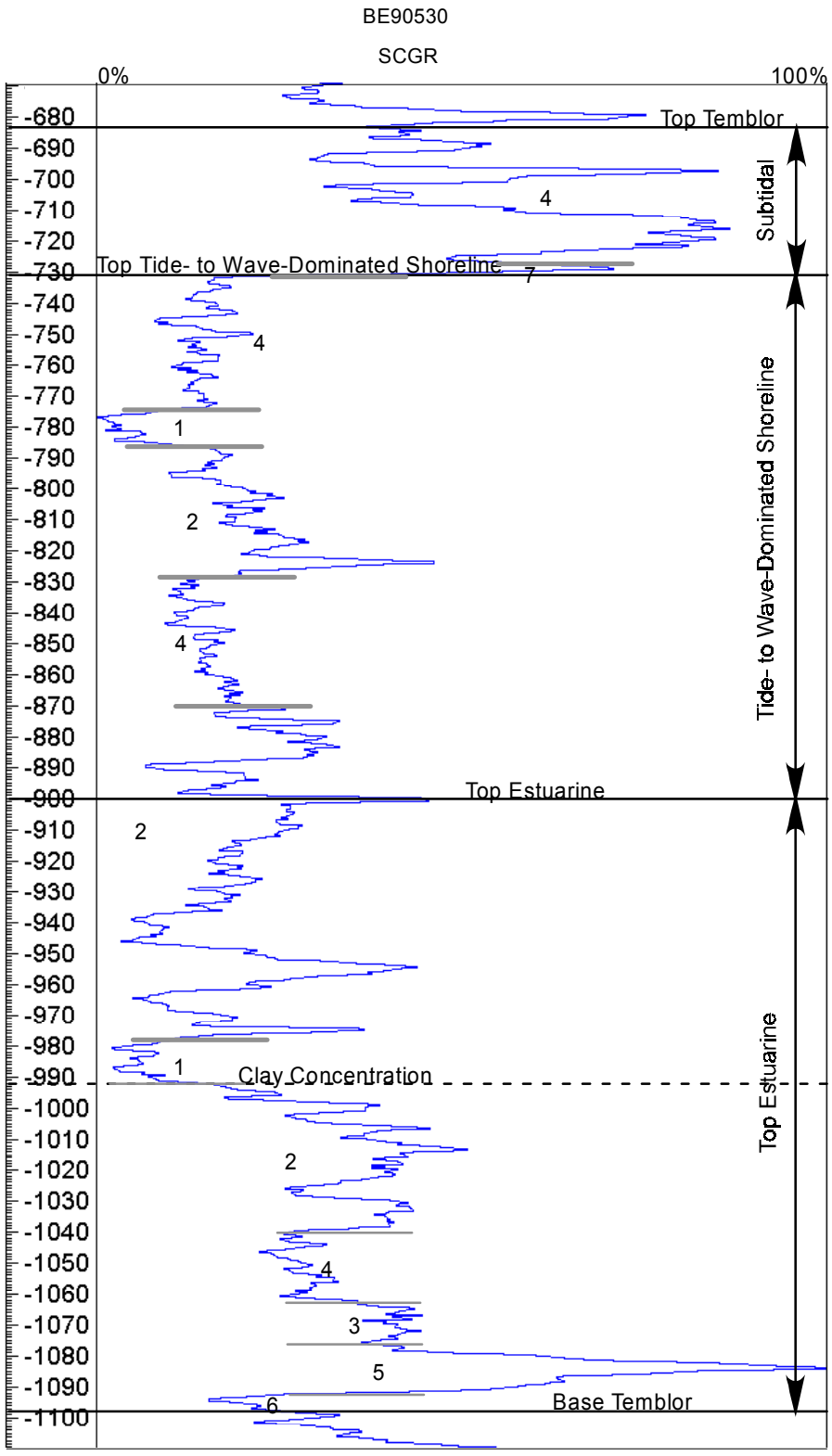

Figure 2. Depositional environments, bounding surfaces, and lithofacies groups listed by number to left of gamma log curve. Well BE90530, Section 25D.

GEOLOGICAL MODELS

Methods

This investigation uses IRAP Reservoir Modeling Software (RMS) for three-dimensional geologic modeling. IRAP RMS was developed by Roxar, Inc. (formerly Smedvig Technologies), for creating three-dimensional models and visualization of reservoirs in the oil and gas industry. The choice of IRAP RMS was based on its ability to integrate multiple data types combined with the high degree of user control. Geologic properties, imported by the user, can be up-scaled and introduced into a flow simulator for enhanced modeling. In addition to the uses in this study, IRAP RMS can also be used to create fault models, lithofacies models, and petrophysical models. Nine major steps were followed for the three-dimensional modeling (Mize, 2002):

1. Collecting, formatting, and sorting data;
2. Loading well data and contouring reference horizons;
3. Generating the reservoir zones and selecting the model resolution by defining the grid structure for each zone;
4. Upscaling (block) the well data to the appropriate resolution for the three-dimensional grid;
5. Creating deterministic models;
6. Defining and modeling the stochastic lithofacies body distributions in each generated zone;

7. Defining and modeling the stochastic petrophysical parameters in each zone and relevant lithofacies;
8. Creating conditioned models;
9. Analyzing the modeling results to determine the types of models best suited for integration with seismic data.

Data formatting included scaling of the raw gamma ray values. This process eliminates calibration differences between logged wells. The resulting scaled gamma ray values are a percentage calculated by the formula:

$$SCGR = \frac{(GR - Min)}{(Max - Min)} * 100 \qquad (1)$$

where

SCGR = the percent of gamma radiation,

GR = the original gamma-ray value for each increment,

Max = the base line for maximum gamma-ray values,

Min = the base line for minimum gamma-ray values.

The minimum value was determined by locating the minimum value for a given gamma-ray log within the interpreted Temblor Formation. The maximum gamma ray value was the highest gamma value within the Temblor Formation, which occurs most often at the base of the subtidal environment.

The process of upscaling wireline log data for this study involves two significant steps: blocking and upscaling. The blocking process identifies every grid block that a well passes through, whereas the upscaling process takes into account the parameter settings and gives each cell a single value. Most wireline log data

have measurements every 0.25 to 1.00 foot. When a grid cell is larger than these increments, the data have to be upscaled or averaged to give each grid cell a single value.

When upscaling discrete logs, each value was assigned a weight or priority, and the lithofacies group value, or score, for each cell was calculated by a weight function:

$$Score = GW * UW \quad (2)$$

where

GW=Geometric Weight

UW=User Weight

The geometric weight is represented by the total length of the well path of the given log type inside the cell in question. The user weight is defined as an integer for each lithofacies group by the investigator. The values are typed in directly by the user. An integer value of 1 would have the greatest weight and would be the dominant lithofacies group. If two or more lithofacies groups have the same score, the lithofacies group with the user determined higher priority would be chosen as the value for that cell. For this investigation, the lithofacies groups that appeared thinner and more continuous in wireline log and core were given the higher priorities.

Structure contour maps were created in RMS for each of the four bounding surfaces: base Temblor, top estuarine, top tide- to wave-dominated shoreline, and top Temblor. A contour map was also created for the clay concentration surface in each section, because it is used for stochastic, deterministic, and conditioned models, though it is not a structural bounding surface. Eight contour maps were

made, four for each study area, using the bounding surfaces that were imported into IRAP RMS as points to create surfaces. The surfaces generally have the same attitude, dipping towards the east-southeast, though this general dip most likely is the result of post-depositional tectonics. Small variations in localized dip direction occur on different bounding surfaces.

Isopach maps were created in RMS for each depositional interval using the isopach gridding function. The isopach maps were created within the software by establishing a top and bottom surface. The software then contours a map of the interval thickness between these two surfaces.

Deterministic models refer to those that use only continuous well data and distribute well properties throughout the model using a weighted moving average to produce a single realization. Deterministic models were created for the scaled gamma ray logs in both study areas. Influence radii of 900 feet in the X and Y directions were used for section 25D, and 25 feet in the Z direction for the estuarine and tide- to wave-dominated shoreline intervals while the subtidal required an influence radius of 800 feet in the X and Y directions, and 20 feet in the Z direction. Influence radii of 1000 feet (X and Y directions) and 75 feet (Z direction) were used in the estuarine and tide- to wave-dominated shoreline for section 36D. The larger Z direction influence radii were used in section 36D to enable the software to interpolate the entire model between the data points. The subtidal zone model was created with an X and Y influence radii of 650 feet and a Z influence radius of 25 feet. The influence radii were established so that the model would be interpolated for all areas not covered by wells.

Stochastic models retain the ability to produce equally probable realizations of subsurface heterogeneity. Two types of stochastic models were created: lithofacies models and petrophysical models. Lithofacies models use upscaled discrete logs (lithofacies groups), and represent the distribution of the different lithofacies types in each zone. A lithofacies model illustrates the spatial relationships among lithofacies bodies and is required before petrophysical or conditioned models can be created.

Petrophysical modeling is used to produce models of a parameter (for example, scaled gamma ray, porosity, permeability, etc.) according to a chosen stochastic lithofacies model using the upscaled well data and lithofacies group parameters. Petrophysical modeling uses the results from lithofacies modeling and produces a set of probabilistic outcomes of parameter distribution (scaled gamma ray in this case) that can be compared in order to evaluate the uncertainty associated with the reservoir description. The two steps involved in creating a petrophysical stochastic model are defining the model job, which establishes the premises for the stochastic simulation, and performing the simulation to obtain the modeling results. Defining the model job involves transforming the scaled gamma ray data into a Gaussian or normal distribution for each zone. After transformations are performed, variograms are created.

Conditioned reservoir models are models in which continuous scaled gamma ray data is interpolated by a weighted moving average for each body modeled in the stochastic lithofacies model. By creating a conditioned model, both the discrete and continuous data are incorporated into the model. Conditioned models are built by

creating a stochastic lithofacies model and deterministically modeling the scaled gamma ray data for each body of the stochastic lithofacies realization.

Modeling Results

Important differences in resolution and accuracy were observed among the four types of models constructed (deterministic, stochastic lithofacies, stochastic petrophysical, and conditioned). These results are summarized in Table 3. Examples of the models are shown in Figures 3 through 10.

The tide- to wave-dominated shoreline interval on all three models of scaled gamma ray (deterministic, petrophysical, and conditioned) has a similar appearance, but the petrophysical and conditioned models are the most similar. There are only a few slight differences at the top of the interval. The estuarine interval of the petrophysical model has scaled gamma ray values that are much lower than those of both the deterministic and conditioned models, which is likely due to the transformation of scaled gamma ray values using the variograms. No major differences are apparent in the subtidal interval of the conditioned model and deterministic models. The estuarine interval is also similar in these two models, except for a few instances where the values of the lithofacies group bodies can be seen. An example of the difference in the models is a single cell layer of low values, roughly 5%, in the estuarine interval of the conditioned model, where there is a layer of moderate values (40 to 55%), just above the –1026 foot elevation line. Similar characteristics are seen in the models and fence diagrams from the section 36D study area.

Table 3: Comparison of the four types of 3D geologic models used in this project.

Model Type	Information/ Observations	Resolution	Advantages for Use	Disadvantages for Use
Deterministic	Continuous (scaled gamma ray) log distribution. Shows truncation of layers at unconformities. Not beneficial to integration with seismic using scaled gamma ray data because it does not incorporate geological interpretation.	Resolution is based on size of the model, usually a few to tens of feet.	Gradational appearance, values more continuous on a large scale compared to petrophysical and conditioned models, models continuous data, would be a sufficient general representation of basic fluid saturation with different data. Different radiation signature in subtidal more evident.	Does not incorporate heterogeneities of lithofacies bodies. Continuity is not realistic. Does not incorporate geologic features, just values represented by logs, Models continuous data only. Continuous distribution is not necessarily accurate.
Stochastic Lithofacies	Shows interconnectivity, size and shape, and lateral and vertical distribution of lithofacies group bodies as defined by input parameters.	Resolution is more detailed than seismic data, but still on the order of 5 to tens of feet within the study areas. Tends to be less detailed when lithofacies bodies are larger.	Incorporates geological aspects of investigation from cores and logs. Takes into account all scales of heterogeneity. Allows several realizations of geology to be observed. Realizations do not vary greatly. Useful tool for prediction of geology. Acceptable model for integration with seismic data.	Model output based solely on input parameters and random insertion. Sharp appearance. Building of models is limited by hardware capabilities (based on size, shape, orientation of bodies, and grid resolution).
Stochastic Petrophysical	Distribution of lithofacies bodies can be seen with assigned continuous well log values assigned to them.	Models do not give an acceptable distribution of scaled gamma ray values given the resolution of this 2000+ x 2000+ foot model. A smaller area might be more acceptable for a petrophysical model.	Uses geostatistical techniques to incorporate discrete and continuous data into one model. With different petrophysical data (sonic or density), this model could be beneficial to a reservoir characterization.	Does not predict geology, but needs accurate lithofacies model for modeling of petrophysical parameters. Values tend to be far (very low) removed from the original continuous log values. Some lithofacies group bodies had scaled gamma ray values that were not correct based on well and core data. Problems in transformation of data.

Table 3 (continued).

Model Type	Information/ Observations	Resolution	Advantages for Use	Disadvantages for Use
Conditioned	Distribution of lithofacies bodies can be seen with assigned continuous well log values. Values in between bodies, where the background lithofacies group occurs, are same as deterministic model.	Resolution is similar to that of deterministic models and is based on the model area and grid structure. Greater variability in scaled gamma ray values is better for representing distribution of values.	Incorporates both deterministic and stochastic models. Models appear more realistic than strict deterministic models by incorporating the lithofacies group bodies. Shows distribution of petrophysical parameters within lithofacies groups.	Values in background lithofacies group average tend to be lower than real scaled gamma ray values. Dependent on accurate lithofacies realization for geological background information. Realizations vary slightly based on lithofacies group realizations.

The lithofacies group objects are used in building the lithofacies, petrophysical, and conditioned models. The lithofacies models clearly show the vertical heterogeneity of lithofacies groups in the study areas. The lithofacies group shapes are apparent in the lithofacies group models, as expected, and are reflected in the petrophysical models. The conditioned model of section 36D shows an abrupt, variable character that does not completely reflect the shapes of the lithofacies group bodies. The estuarine interval has several grid blocks that are of a slightly different value than expected, but do not reflect the shape of a body. Some of the same characteristics of bodies occur in both the petrophysical and conditioned models near the base of the estuarine interval where there is a large area of background lithofacies group (burrowed sand, in this case), whose value is reflected in its shape on the lithofacies group model.

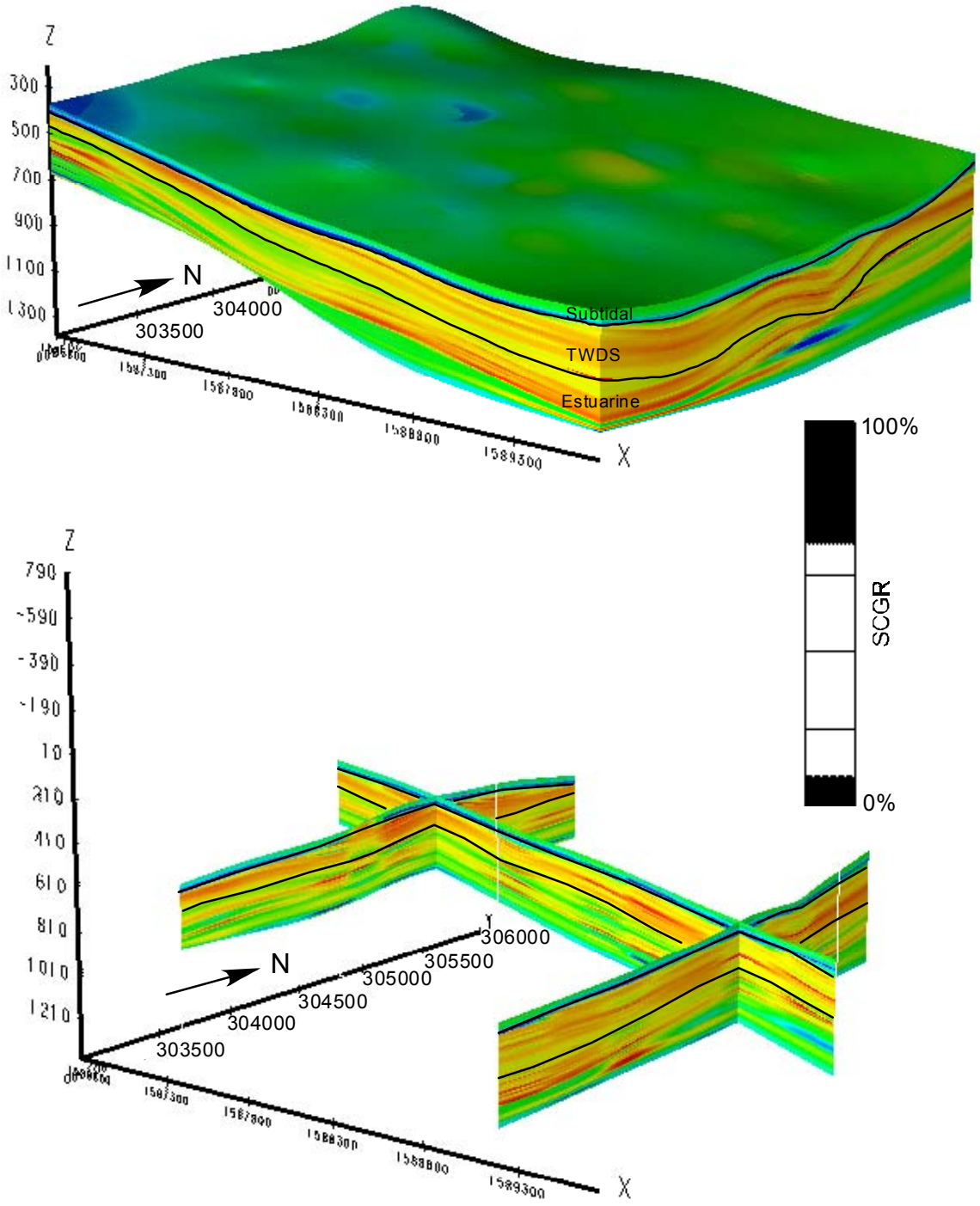

Figure 3: Deterministic model and cross sections for study area in section 25D. TWDS=tide- to wave-dominated shoreline.

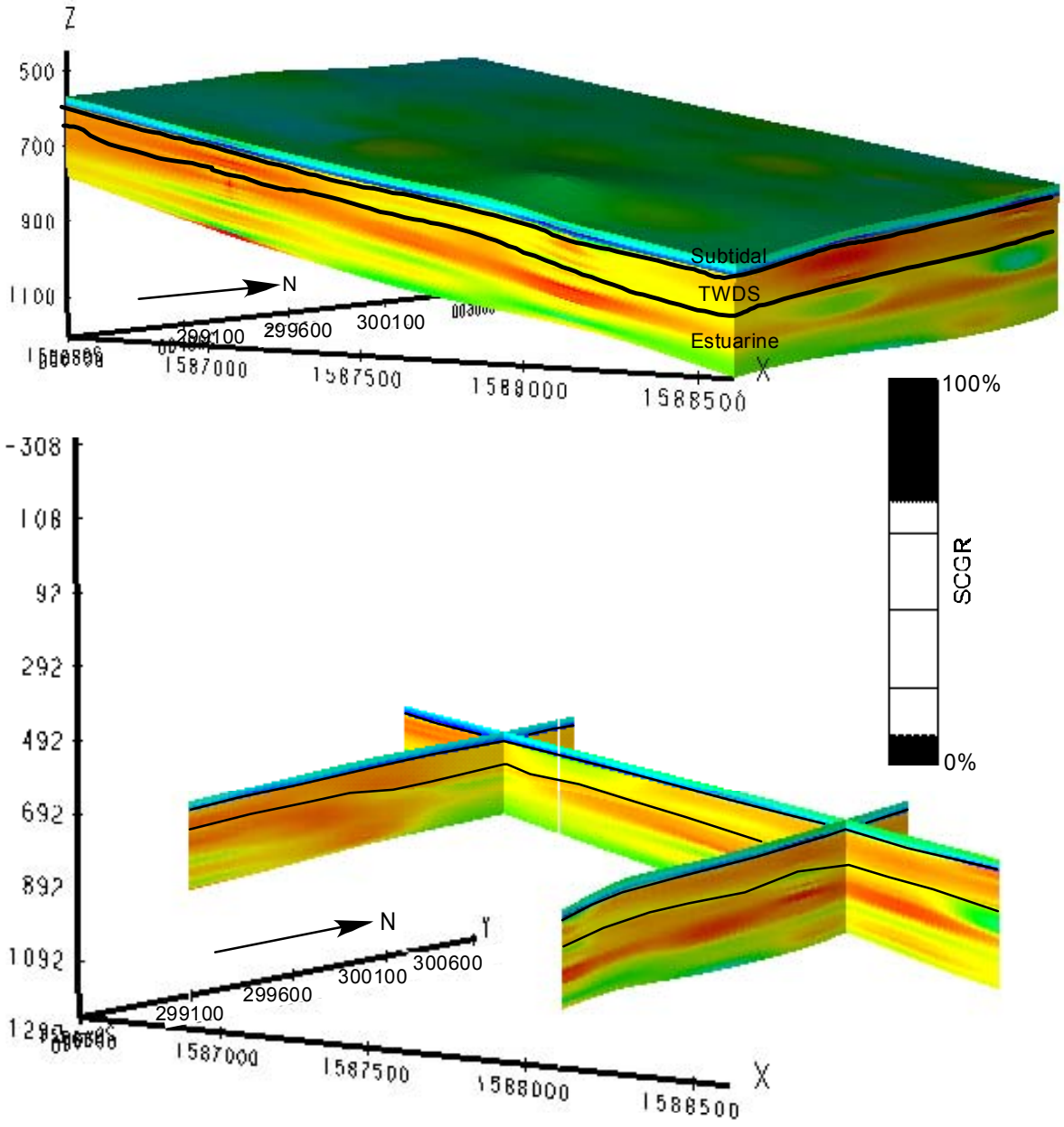

Figure 4: Deterministic scaled gamma ray model and cross sections for study area in section 36D. TWDS=tide- to wave-dominated shoreline.

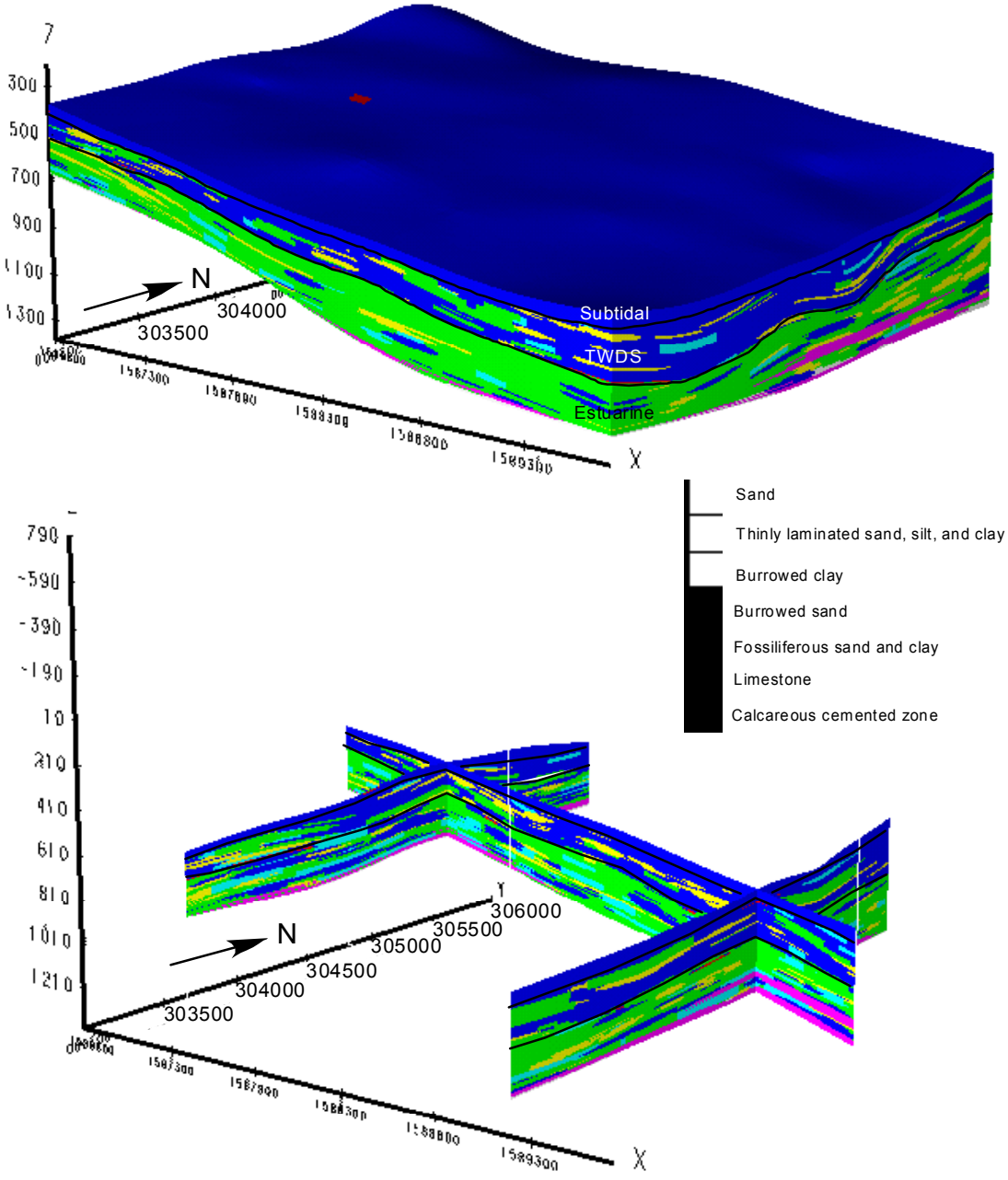

Figure 5: Stochastic lithofacies model and cross sections for study area in section 25D. TWDS=tide- to wave-dominated shoreline.

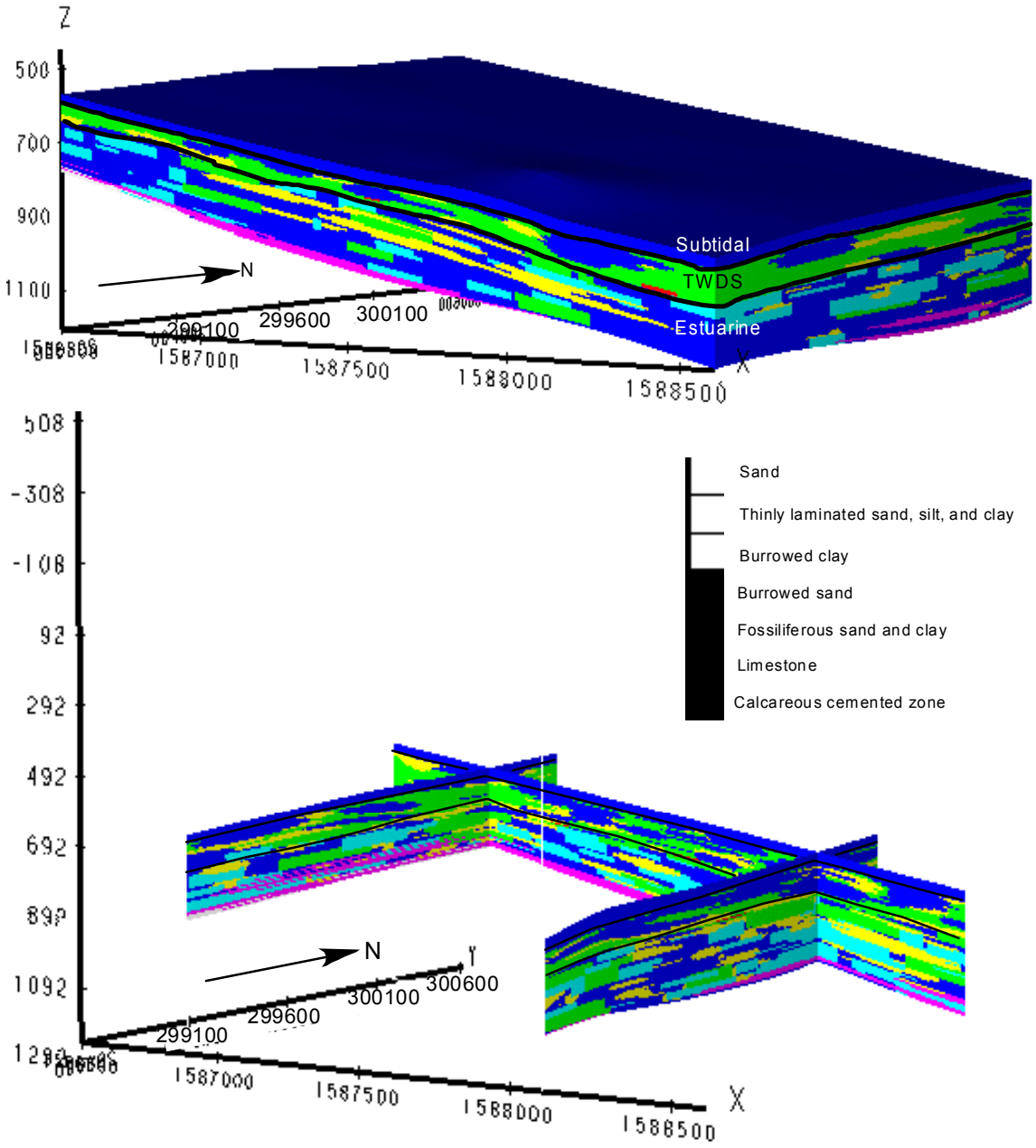

Figure 6: Stochastic lithofacies model and cross sections for study area in section 36D. TWDS=tide- to wave-dominated shoreline.

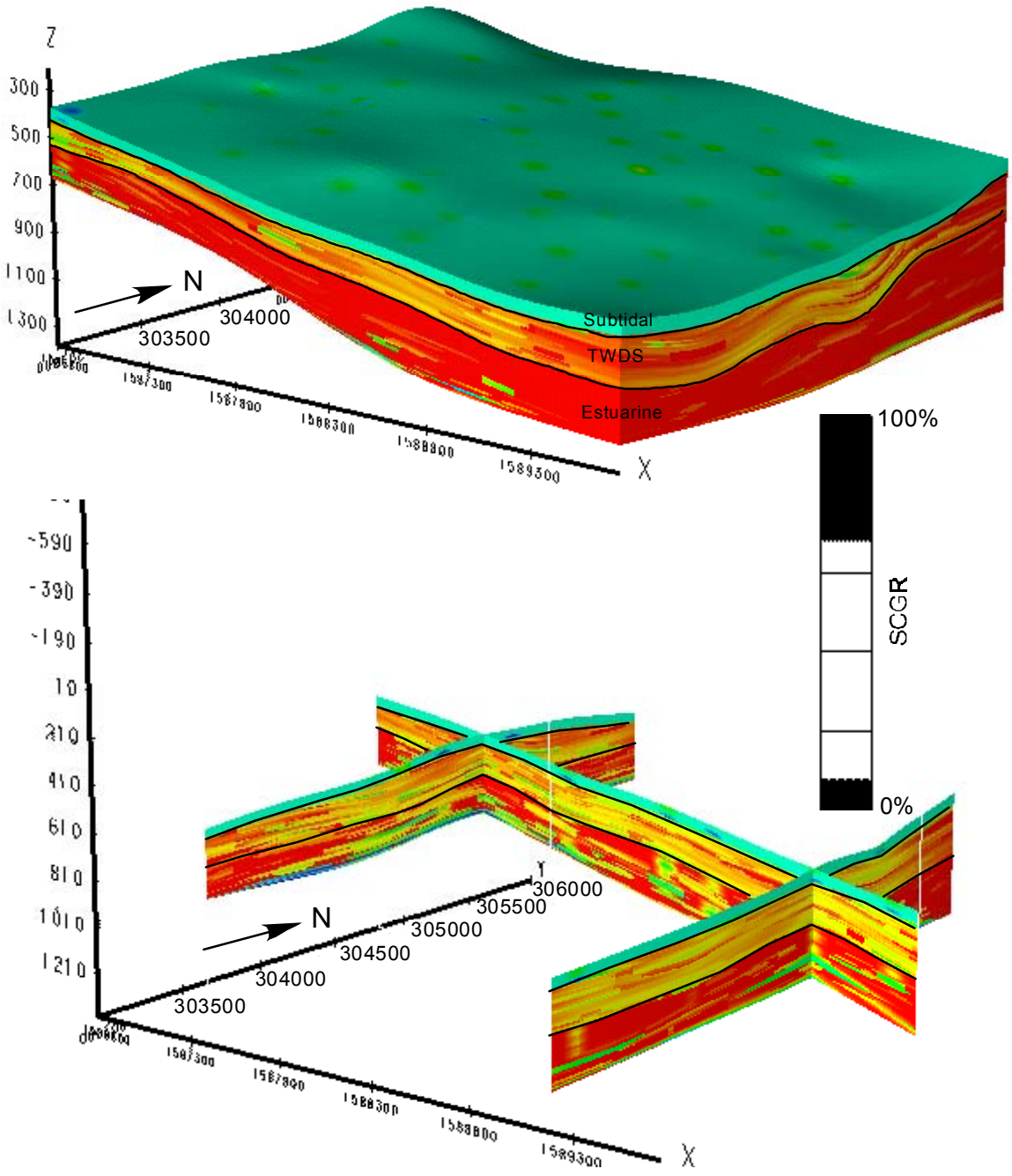

Figure 7: Petrophysical model and cross sections for study area in section 25D. TWDS=tide- to wave-dominated shoreline.

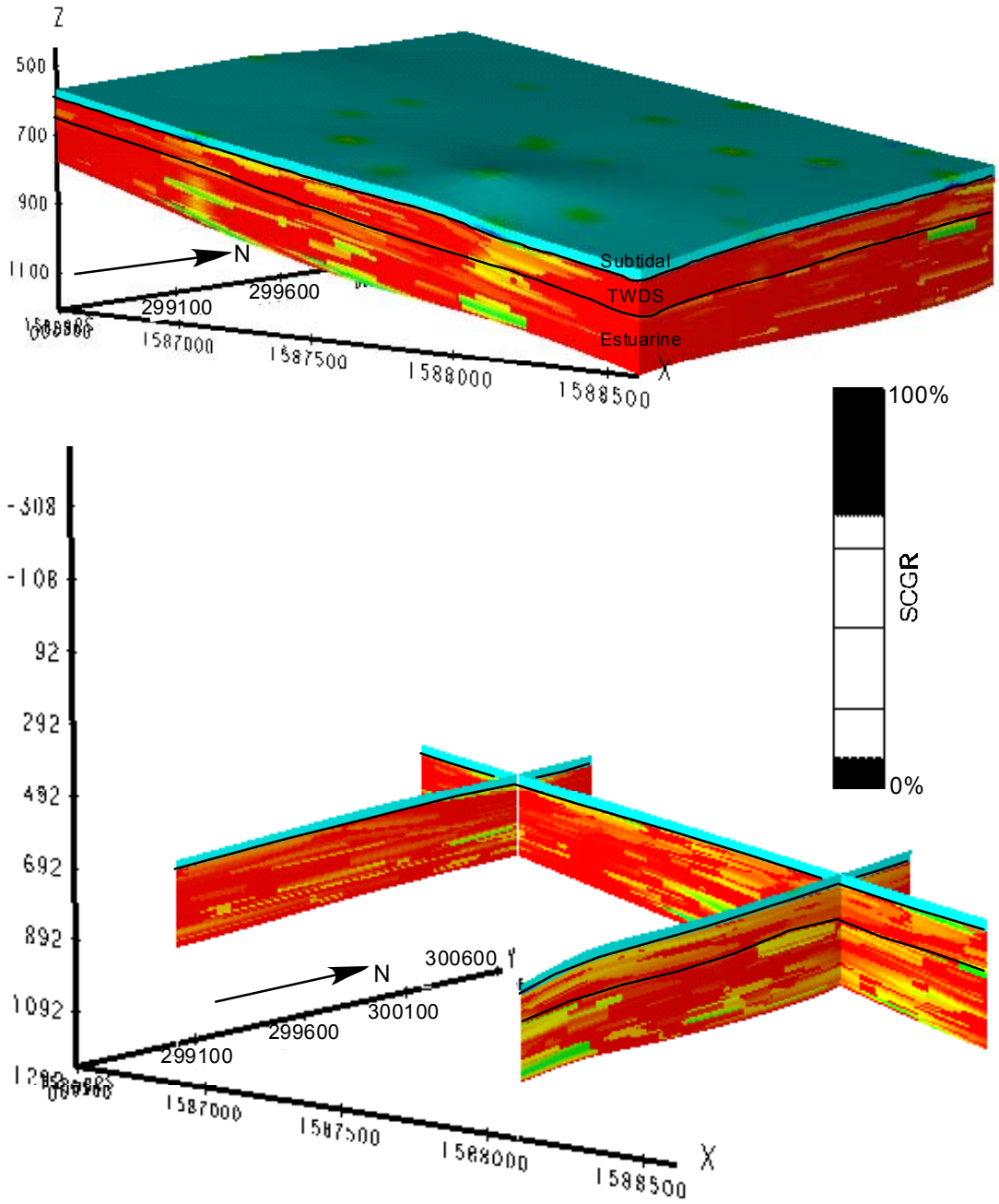

Figure 8: Petrophysical model and cross sections for study area in section 36D. TWDS=tide- to wave-dominated shoreline.

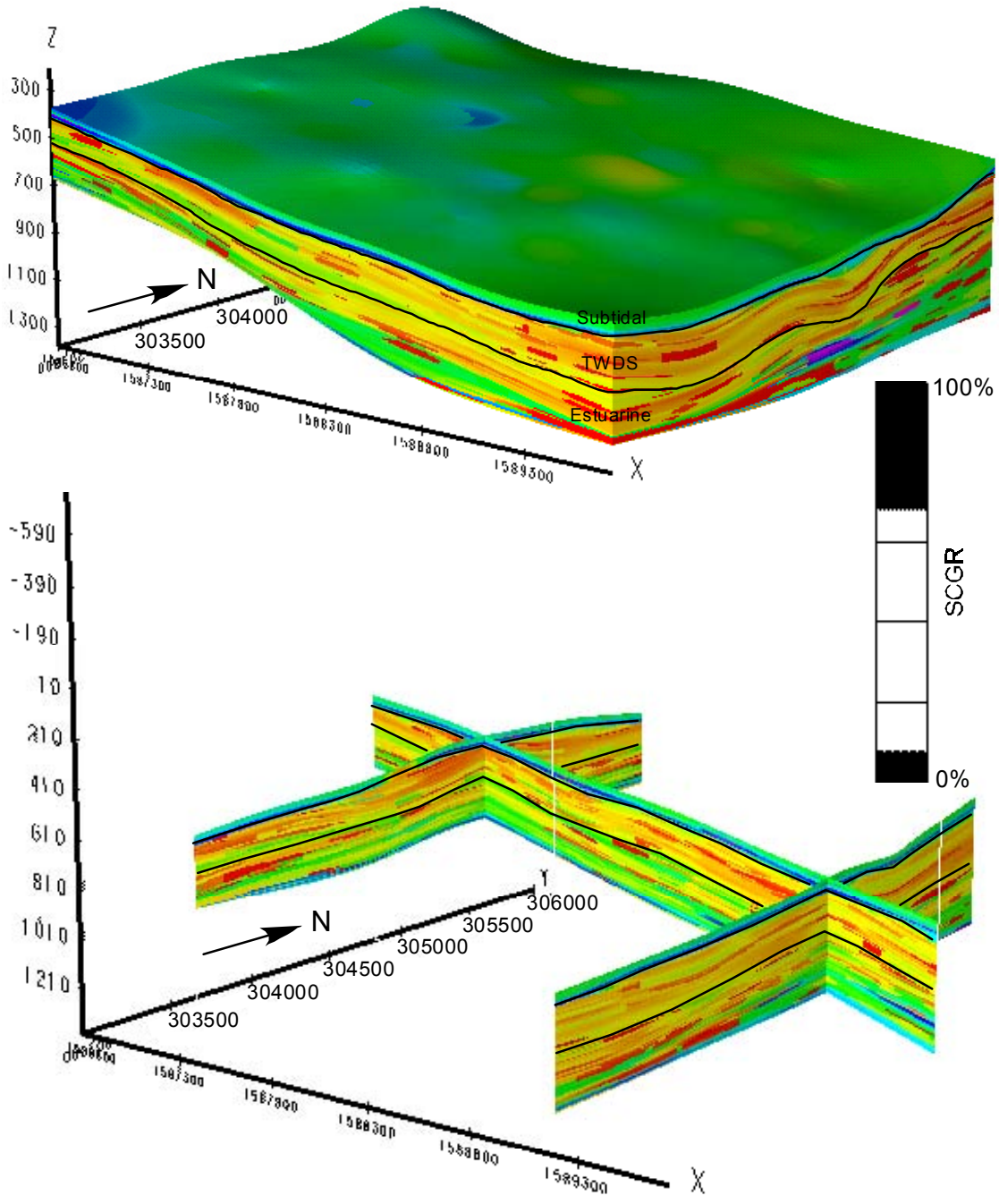

Figure 9: Conditioned model and cross sections for study area in section 25D. TWDS=tide- to wave-dominated shoreline.

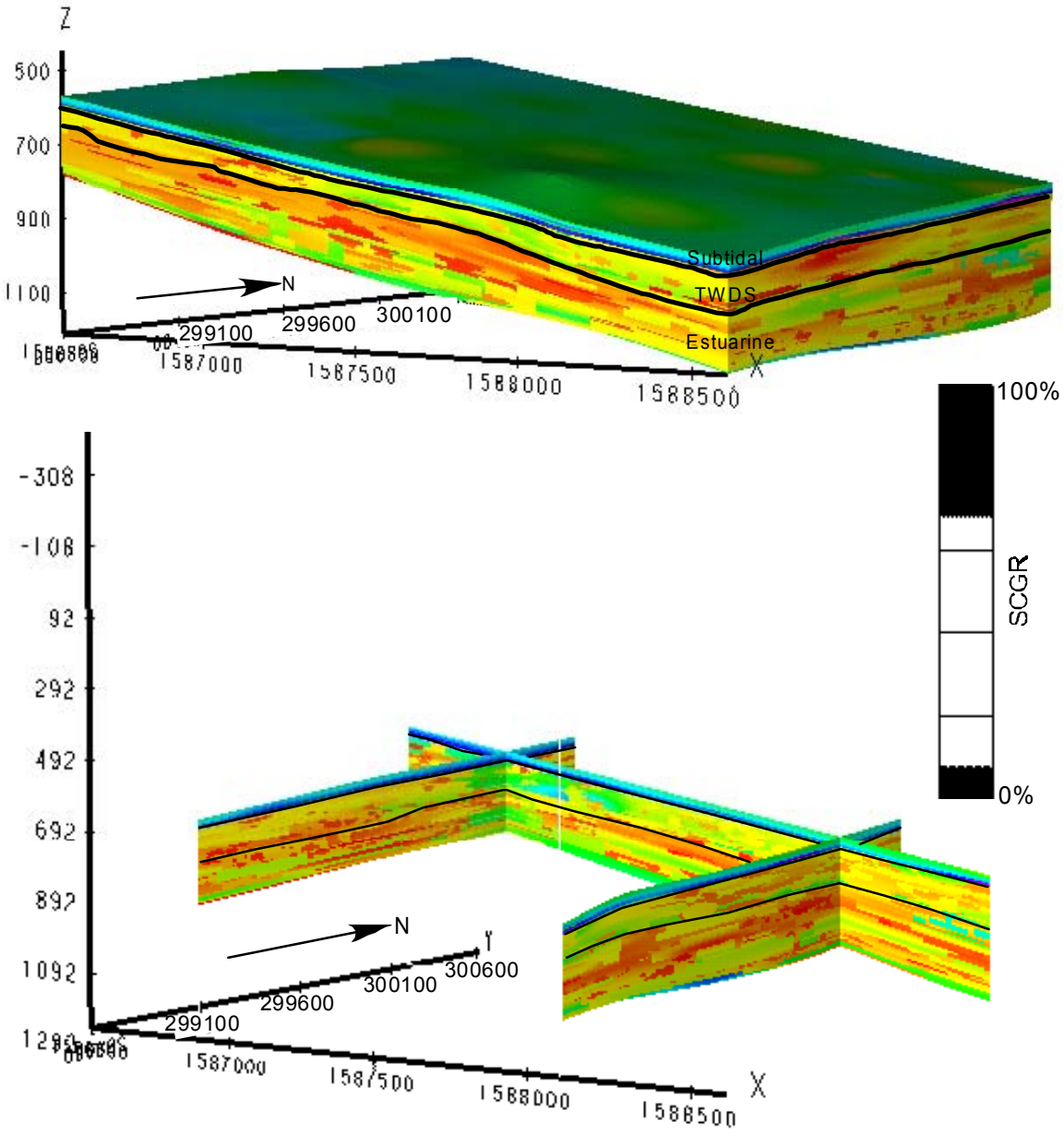

Figure 10: Conditioned scaled gamma ray model and cross sections for study area in section 36D. TWDS=tide- to wave-dominated shoreline.

CONCLUSIONS

The stochastic lithofacies models and conditioned models are the most suitable types of models (of the 4 methods tested) for integration with seismic data. Deterministic models exhibit a smooth interpolation of the continuous scaled gamma ray values, which may not be an accurate depiction of the subsurface geology because of heterogeneity. There is not a high degree of lateral continuity in the two study areas, so a strict interpolation technique as used in the deterministic models is not the best method to use for the discrete data. Stochastic models use the data to statistically define the spatial parameters, whether they are geological or petrophysical.

The stochastic lithofacies models incorporate the geologic characteristics of the subsurface as revealed in core and interpreted from wireline logs by creating multiple realizations, which statistically have the same likelihood of occurring. The lateral and vertical heterogeneity of the Temblor Formation is depicted by the distribution of lithofacies group bodies in realizations of the stochastic lithofacies, which is supported by cores and wireline logs. There are some small areas, usually near the margins of the study areas, which may be less accurate due to the random placement of objects caused by the lack of data.

Petrophysical models are strongly influenced by distribution of the lithofacies group objects. The calculations of scaled gamma ray values are performed in each of the individual lithofacies group bodies to simulate small-scale variations in scaled gamma ray values. The method allows a representation of scaled gamma ray values

in between the wells. The incorporation of geology is a good reason for using petrophysical models with seismic data. However, the values in the final petrophysical models do not always correspond with the expected values of the lithofacies bodies as determined from wireline logs. With the use of petrophysical parameters such as oil saturation, grain size, porosity, and/or permeability, a more useful model could probably be created.

The conditioned models combine the information from both the lithofacies models and the deterministic scaled gamma ray models. The incorporation of discrete geologic parameters and the continuous petrophysical parameters show the distribution of the continuous scaled gamma ray parameter based on geological realizations. The values assigned to the lithofacies group bodies and the background parameters are consistent with the original continuous log values. This method is useful when modeled with scaled gamma ray logs, but could possibly become even more useful if other logs, such as density, were incorporated.

REFERENCES

Bridges, R.A., 2001, *Sedimentology and reservoir characterization of the Miocene Temblor Formation, Coalinga, California* [unpublished Master's thesis]: Clemson University, 114 p.

Bridges, R.A., and J.W. Castle, 2002, Local and regional tectonic control on sedimentology and stratigraphy in a strike-slip basin: Miocene Temblor Formation of the Coalinga Area, California, U.S.A." *Sedimentary Geology*, in press.

Castle, J.W., F.J. Molz, R.W. Falta, C.L. Dinwiddie, S.E. Brame, R.A. Bridges, 2002, *Quantitative Methods for Reservoir Characterization and Improved Recovery: Application to Heavy Oil Sands*, Final Technical Report for Contract DE-AC26-98BC15119, USDOE, 78 p.

Mize, K.L., 2002, *Development of three-dimensional geological modeling methods using cores and geophysical logs, West Coalinga Field, California* [unpublished Master's thesis]: Clemson University, 202 p.